Fault Friction Derived From Fault Bend Influence on Coseismic Slip During the 2019 Ridgecrest Mw 7.1 Mainshock

JGR Solid Earth

RESEARCH ARTICLE
10.1029/2022JB024519

Fault Friction Derived From Fault Bend Influence on Coseismic Slip During the 2019 Ridgecrest M_w 7.1 Mainshock

C. W. D. Milliner[1], S. Aati[1], and J. P. Avouac[1]

[1]California Institute of Technology, Pasadena, CA, USA

Key Points:

- Inverting surface coseismic slip vectors show a variable stress state that matches the background stresses constrained by seismicity
- Faults at the mainshock epicenter were the most critically stressed; we find slip increases linearly as faults become more optimally aligned
- We find absolute stress magnitudes of 8–26 MPa in the upper crust, a static frictional coefficient of 0.61 and a dynamic value of 0.29

Supporting Information:

Supporting Information may be found in the online version of this article.

Correspondence to:

C. W. D. Milliner,
milliner@caltech.edu

Citation:

Milliner, C. W. D., Aati, S., & Avouac, J. P. (2022). Fault friction derived from fault bend influence on coseismic slip during the 2019 Ridgecrest M_w 7.1 mainshock. *Journal of Geophysical Research: Solid Earth*, *127*, e2022JB024519. https://doi.org/10.1029/2022JB024519

Received 1 APR 2022
Accepted 16 OCT 2022

Author Contributions:

Conceptualization: C. W. D. Milliner
Data curation: C. W. D. Milliner
Formal analysis: C. W. D. Milliner, S. Aati, J. P. Avouac
Funding acquisition: C. W. D. Milliner, J. P. Avouac
Investigation: C. W. D. Milliner, J. P. Avouac
Methodology: C. W. D. Milliner, S. Aati, J. P. Avouac
Project Administration: C. W. D. Milliner, J. P. Avouac
Resources: C. W. D. Milliner, J. P. Avouac
Software: C. W. D. Milliner, S. Aati
Supervision: J. P. Avouac
Validation: C. W. D. Milliner
Visualization: C. W. D. Milliner
Writing – original draft: C. W. D. Milliner

Abstract The variation of stress on faults is important for our understanding of fault friction and the dynamics of earthquake ruptures. However, we still have little observational constraints on their absolute magnitude, or their variations in space and in time over the seismic cycle. Here we use a new geodetic imaging technique to measure the 3D coseismic slip vectors along the 2019 Ridgecrest surface ruptures and invert them for the coseismic stress state. We find that the coseismic stresses show an eastward rotation that becomes increasingly transtensional from south-to-north along the rupture, that matches the known background stress state. We find that the main fault near the M_w 7.1 mainshock hypocenter was critically stressed. Coseismic slip was maximum there and decreased gradually along strike as the fault became less optimally oriented due its curved geometry. The variations of slip and stress along the curved faults are used to infer the static and dynamic fault friction assuming Mohr-Coulomb failure. We find shear stresses of 4–9 MPa in the shallow crust (~1.3 km depth) and that fault friction drops from a static, Byerlee-type, value of 0.61 ± 0.14 to a dynamic value of 0.29 ± 0.04 during seismic slip. These values explain quantitatively the slip variations along a transpressional fault bend.

Plain Language Summary Understanding the orientation and magnitude of stresses within the crust are important because they can affect the location, size and spatial extent of earthquake rupture. However, measuring the absolute magnitude and orientation of stresses as well as the frictional properties of the fault surface (i.e., how strongly the fault resists the applied driving forces) is very difficult. Here we use optical images acquired by satellites to measure how the surface deformed in 3D during the 2019 Ridgecrest event. These 3D measurements allow us to extract the direction of fault slip movement along the entire rupture length which we use to estimate the direction of stresses by assuming the shear stress is parallel to the direction of the observed fault slip motion. We find that the main fault near the mainshock epicenter was the most optimally aligned for failure, which could be one contributing reason for the location of rupture initiation. By deriving a relation between how much a fault slips with how well aligned it is to the stress field we can estimate the absolute magnitude of stresses, the frictional resistance at initial fault sliding (finding a static friction = 0.61) and during sliding (a dynamic friction = 0.29).

1. Introduction

Earthquakes are frictional slip instabilities which initiate when the applied shear stress exceeds the yield strength of the fault. During sliding the friction can increase (dynamic strengthening) or decrease (dynamic weakening), where the former inhibits rupture, and the latter can sustain a runaway failure which relieves a fraction of the accumulated stress along the fault surface. During the interseismic period the elastic stresses re-accumulate along the locked fault surface until the fault strength is reached again and another earthquake occurs. This basic description of the seismic cycle underlines the importance of fault strength in our understanding of when and how earthquakes occur. However, outstanding questions remain regarding the strength of faults including, is the frictional strength substantially lower during rupture than the static strength expected for a standard value of the static coefficient of friction (the ratio of the shear to normal stress which is generally around 0.6 for most rocks) (Byerlee, 1978)? If so, what is the extent of dynamic weakening? Are faults inherently weak or are intracrustal faults stronger than their more mature plate boundary counterparts? In this study we attempt to place empirical constraints on these important fault mechanical properties using observations of a surface rupturing event provided by satellite imaging data.

The 2019 Ridgecrest earthquake sequence initiated on 4 July by a series of foreshocks which later ruptured a series of orthogonal faults near the city of Ridgecrest located north of the Mojave Desert (Ross et al., 2019). First,

Writing – review & editing: C. W. D. Milliner, J. P. Avouac

a M_w 6.4 event ruptured a dextral NW-trending fault at depth and a sinistral NE-trending fault at the surface. This was then followed ∼34 hr later by the M_w 7.1 mainshock that initiated ∼15 km to the north. During the mainshock event, kinematic source models show a transition from an initially crack-like to pulse-like bi-lateral rupture (Figure 1). The rupture then evolved to an unilateral slip pulse which propagated southeastwards at a relatively slow velocity of ∼2 km/s along a curved 19° compressional fault bend (Figure 1c) (Chen et al., 2020; Goldberg et al., 2020; Ross et al., 2019). Measurements made in the field or from satellite image correlation (Antoine et al., 2021; Barnhart et al., 2019; DuRoss et al., 2020; Gold et al., 2021; Milliner & Donnellan, 2020; Ponti et al., 2020) show a gradual decrease of coseismic slip (∼2.5 m over a ∼5 km distance) southwards and away from the mainshock epicenter along the curved fault geometry (see fault bend location in Figure 1). In this study, we analyze how this feature relates to fault stress and show that some information on fault friction can be derived.

Previous studies using focal mechanisms from background seismicity and aftershocks have provided estimates of the state of stress in the crust around the Ridgecrest region, including its spatial variation along the foreshock and mainshock ruptures and its change with time. Inversion of focal mechanisms from background seismicity prior to the 2019 earthquake sequence shows a strike-slip stress regime along the faults involved in the mainshock rupture (where the intermediate compressive principal stress [σ_2] is approximately vertical) with some spatial variations along-strike (Hardebeck, 2020; Hauksson et al., 2020; Sheng & Meng, 2020; X. Wang & Zhan, 2020). The maximum principal stress, σ_1, is near-horizontal and rotates from due North at the southern end of the mainshock rupture to ∼N12°E in the north. The stress shape ratio (R), which characterizes the relative magnitudes of the principal stresses and is defined as $R = [\sigma_1 - \sigma_2]/[\sigma_1 - \sigma_3]$), also spatially varies and indicates an increasingly transtensional stress regime to the north. Here we attempt to assess how spatially variable the stresses are that are released along a rupture and whether this supports the notion of heterogeneity of the stress orientation at the ten's of kilometers scale in the surrounding crust that is typically inferred from background seismicity.

Hereafter we introduce the tectonic setting of the Ridgecrest earthquake sequence. We next present the methods used in this study. We use a newly developed optical image correlation technique to measure the 3D slip vectors along the 2019 Ridgecrest earthquake sequence (Figures 1a and 1b) and invert these to determine the orientation and shape of the 3D deviatoric stress tensor to understand its spatial variability. We next present our results and implications. We use the coseismic stress state to assess the influence of fault strength excess, the difference between the critical shear stress (often referred to as the yield shear stress) needed for slip to occur and the initial shear stress. We show that, as expected from theory, the more critically stressed faults released a larger amount of coseismic slip (e.g., Aochi et al., 2002; Kase & Day, 2006). From assuming a Mohr-Coulomb failure criterion, we are then able to estimate the absolute magnitude of the principal stresses as well as the static and dynamic friction coefficients.

1.1. Tectonic Setting

The 2019 Ridgecrest earthquake sequence occurred between the transition of the 160-km wide Eastern California Shear Zone (ECSZ) located to the south and the Walker Lane located to the north which both accommodate northwest-trending dextral shearing of up to ∼25% of the Pacific–North America plate boundary motion (Dixon et al., 2000; Hammond & Thatcher, 2004; McClusky et al., 2001; Rockwell et al., 2000). Both tectonic regions have hosted three major historical earthquakes, including the 1873 Owens Valley earthquake located 45 km to the north of the Ridgecrest rupture, and the 1992 M_w 7.3 Landers and 1999 M_w 7.1 Hector Mine events, both located ∼110 km to the southeast in the Mojave Desert. These events likely reflect the accommodation of distributed dextral strain within the continental interior caused by the transfer of Pacific-North American plate boundary motion away from the San Andreas fault, located to the west, as it bends westward north of the Transverse ranges (Bennett et al., 2003; Faulds et al., 2005; Wesnousky, 2005).

The unusual rupture of faults with orthogonal and mechanically unfavorable orientations during the 2019 Ridgecrest earthquake sequence have been thought to arise from crustal rotation caused by regional dextral simple shear strain. Such crustal rotations were observed in the current interseismic crustal velocity field using GNSS (Fialko & Jin, 2021). Although there is currently limited constraint of the paleoseismic history of the faults involved in the 2019 rupture sequence, it is thought that they are structurally immature due to the slow velocity of the mainshock rupture (Chen et al., 2020; Goldberg et al., 2020; Ross et al., 2019; K. Wang et al., 2020), the relatively unorganized fracture pattern (Ponti et al., 2020), wide zone of coseismic inelastic finite strain

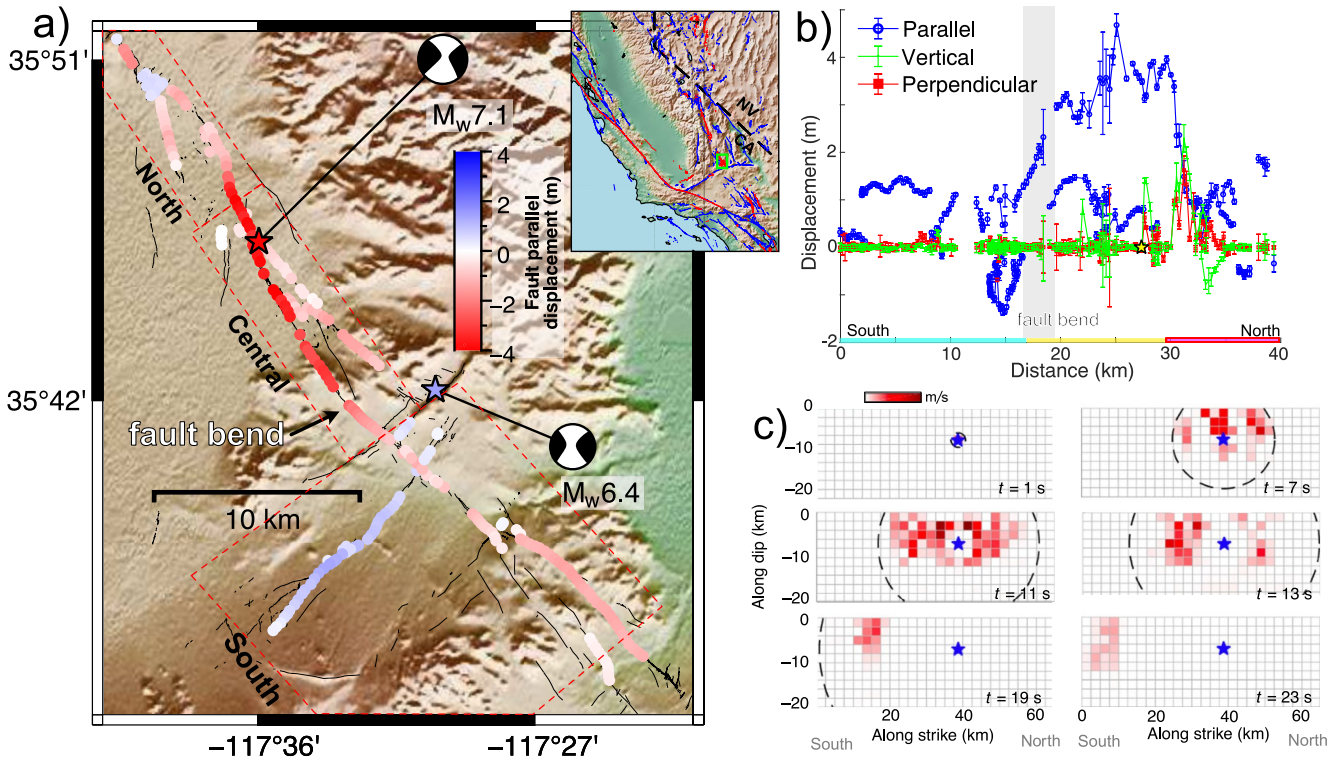

Figure 1. Coseismic slip vectors and rupture kinematics. Panel (a) fault-parallel component of slip measured from optical image correlation. Red dashed boxes correspond to the three stress zones. (b) Slip distribution illustrating the fault-parallel (blue, where negative denotes left-lateral slip), perpendicular (red) and vertical (green) along the direction of the mainshock surface rupture measured from the 3D deformation maps (see Figure S1 in Supporting Information S1), star shows epicenter location. Cyan, yellow and magenta horizontal bars at bottom denote the extent of the southern, central and northern zones, respectively. Change of fault strike associated with rupture bend is denoted by vertical gray bar. (c) Rupture kinematics of the M_w 7.1 mainshock constrained by inversion of seismic and geodetic data, which illustrates the transition from initial crack-like to pulse-like rupture, viewing southwest, panel adapted from Chen et al. (2020).

(Antoine et al., 2021; Milliner et al., 2021) and relatively low cumulative displacements (0.3–1.6 km) (Andrew & Walker, 2020; Milliner et al., 2021).

2. Methods

2.1. Measuring 3D Surface Deformation Using Optical Image Correlation

To measure the tectonic surface deformation pattern we use a new optical image correlation technique that we have developed called COSI-Corr$^+$ (Aati et al., 2022). We apply this open-source and automated image processing technique for the first time to resolve the full 3D deformation field of the Ridgecrest earthquake sequence as this method offers a number of benefits over current image matching approaches.

Standard image correlation resolves the 2D horizontal displacement with sub-pixel precision typically by applying a frequency correlation scheme, which is based on the principal that a translation in space is equivalent to a shift in phase in the Fourier domain (Avouac & Leprince, 2015; Leprince et al., 2007). More recently a number of matching approaches have been developed to resolve the full 3D deformation pattern (i.e., additionally measuring the vertical component of surface motion) using geodetic imaging datasets. The iterative closest point algorithm (ICP) is such an approach that is typically applied to pre- and post-event point clouds acquired by airborne or terrestrial lidar (Besl & McKay, 1992; Nissen et al., 2012). ICP solves for the 3D deformation field by iteratively solving for a local rigid-body transformation (translation and rotation) that minimizes the square sum of the distances between a tangential plane of a reference point and its paired point in the target tile.

The most common method for solving the 3D surface deformation using optical satellite or aerial images is to solve independently for the horizontal and vertical deformation components, which we refer to as the "2 + 1D" approach. Here in-track stereo image pairs are required both before and after an earthquake in order to produce

pre- and post-digital elevation models (DEM). The pre- and post-raw images are then orthorectified with the respective DEM's and the 2D horizontal component of surface motion is determined using a standard image correlation technique. The vertical component is then estimated by differencing the two DEMs which are aligned to one another by accounting for the lateral translation provided by the horizontal deformation result (Avouac & Leprince, 2015).

Although these approaches have wide use, the accuracy of the resulting deformation maps can be affected by a number of factors. The ICP approach requires an estimate of the local surface normal, which makes it highly sensitive to noise in the point cloud which is dependent upon the DEM quality. This requires smoothing to help remove outliers that results in loss of spatial resolution and details of the deformation pattern. Second, the ICP matching result may not always reflect the true 3D displacement. This can occur in regions of low relief as the ICP method attempts to find the closest Euclidean distance between point clouds that has no independent constraint of the amount or direction of lateral translation, thereby making it susceptible to biases such as apparent topography. For optical image matching techniques, both the traditional 2D and "2 + 1D" approaches typically contain orthorectification, topographic, satellite jitter, sensor array and aliasing artifacts that can all contaminate the final deformation result.

The new COSI-Corr$^+$ algorithm offers several advancements that addresses some of the aforementioned issues affecting current matching approaches. First, this includes optimization of the rigorous sensor model (RSM), which contains information of the satellite velocities, positions, attitudes and sensor orientations. Refinement of the RSM parameters is performed by optimizing the locations of a set of ground control points with an orthorectified reference data set. This refinement leads to a more accurate estimate of the satellite look vector to each image pixel location thereby helping reduce registration and orthorectification artifacts. Second, we have implemented a ray tracing step, which is used to invert for the intersection of the various satellite look directions and triangulate the 3D position of each image pixel. Knowing the 3D location of each pixel from all images acquired before and after the earthquake along with the amount of translation between every image pair, that is determined by the image correlation step, then allows us to solve for and separate apparent surface motion caused by the 3D tectonic deformation from translation caused by the parallax effect due to topography. Finally, as a post-processing step we apply an independent component analysis (ICA) to the deformation maps, which is a multivariate statistical technique that deconstructs a data set into a set of statistically independent sources (Gualandi et al., 2016). ICA is used to separate and isolate the tectonic signal—which is a source common to all of the image correlations—from sensor artifacts, which are sources associated with specific images. The new COSI-Corr$^+$ technique also offers the advantage in that the final deformation results are insensitive to the type or resolution of the DEM used and is flexible in that it can process optical images acquired by different satellite platforms. The latter is especially useful as it provides a greater number of satellite look vectors with which to more accurately triangulate the 3D position of pixels. Additional processing details are described in Aati et al. (2022).

The general COSI-Corr$^+$ workflow involves five main steps, this includes (a) the RSM refinement, (b) image orthorectification and resampling, (c) sub-pixel image correlation, (d) 3D displacement calculation via ray tracing and (e) deconstruction of the 3D deformation maps with ICA (for additional details see Aati et al. [2022]). This workflow results in a final set of three deformation maps where the surface motion is decomposed into the east-west, north-south and vertical component of motion (see Figure S1 in Supporting Information S1).

To measure the surface deformation field we processed 26 WorldView-1 (0.55 m pixel resolution), 32 WorldView-2 (0.55 m pixel resolution), 30 WorldView-3 (0.36 m pixel resolution), and two SPOT satellite images (1.5 m pixel resolution), where we used 113 orthorectified aerial images (0.6 m resolution) as the reference data set. These satellite images span a time frame between 2016 and 2021 (see Table S1 in Supporting Information S1 for details). To determine the uncertainty of the deformation maps we measured the surface motion in a far-field, stable region away from the coseismic ruptures. Here we find the uncertainty in the east-west, north-south, and vertical directions is 0.7, 0.6 and 0.6 m at the 90% confidence level, respectively. This processing workflow results in a significant reduction of topographic, orthorectification, and CCD array artifacts (with a reduction of uncertainty in the deformation maps by a factor of ~3.6 compared to a result using the traditional "2 + 1 D approach"), and near complete removal of aliasing artifacts associated with the SPOT 6 images (see Aati et al. [2022] for details).

To then measure the coseismic slip vectors along the rupture from the 3D deformation maps we used stacked profiles orientated across the foreshock and mainshock ruptures. This allows us to measure the magnitude of the total differential surface motion in the fault-parallel, perpendicular, and vertical directions (see Figure S2 in

Supporting Information S1). This approach gives the advantage of providing an estimate of the total fault offset magnitude across the rupture that is not affected by the amount of distributed off-fault strain that can vary along the rupture. If distributed off-fault strain was not accounted for it would lead to an underestimation of the total fault offset that would bias our understanding of how stress affects the along-fault variation of the coseismic slip magnitude. The coseismic slip vectors were then constructed from the total offset in the three components of motion, which were measured every 138 m along the rupture across 24 different fault strands. This resulted in a total of 240 slip vector measurements (see Figure 1). The slip vectors exhibit a diverse range in rake, with left-lateral slip along the foreshock rupture, right-lateral slip along the majority of the mainshock rupture, and near it's northern termination we find left-lateral slip along conjugate faults and oblique dextral-normal slip (see Figure S2 in Supporting Information S1). Comparing the coseismic slip vectors measured here with those from other studies using standard geodetic image matching techniques shows very strong agreement for the horizontal component (with a correlation coefficient of 0.97, see Figure S3 in Supporting Information S1) (Gold et al., 2021; Morelan & Hernandez, 2020). In addition, the vertical component of slip that we measure shows good qualitative agreement with that observed in field surveys. For example, regions of subsidence near the northern termination of the mainshock rupture occurs along a known graben structure and subsidence that we resolve along multiple right-releasing transtensional bends of the mainshock rupture were also observed by field mapping surveys (DuRoss et al., 2020; Ponti et al., 2020).

2.2. Coseismic Slip Vector Inversion for Stress Orientation

To estimate the 3D deviatoric stress tensor, we invert the unit slip vectors under the Wallace-Bott assumption that slip is parallel to the shear stress (Michael, 1984). The stress inversion provides an estimate of the orientation and shape of the 3D deviatoric stress tensor but not its magnitude. A similar approach was previously applied using field surface observations following the 2010 M_w 7.1 El-Mayor Cucapah earthquake (Fletcher et al., 2016). Here we use measurements from optical image correlation that provides spatially dense and regular measurements of slip along the entire Ridgecrest surface rupture that allows constraint of the spatial variation of the stress state. The principal deviatoric stresses, $\sigma_1, \sigma_2, \sigma_3$ are ordered from most to least compressive and the shape of the tensor is quantified from $R = [\sigma_1 - \sigma_2]/[\sigma_1 - \sigma_3]$). Under a strike-slip stress regime where σ_2 is vertical, a value of $R = 0$ signifies a transtensional regime, $R = 0.5$ a purely strike-slip regime and $R = 1$ a transpressional regime. To resolve spatial variations of stress along the rupture we distinguish three zones from NNW-to-SSE along the mainshock rupture, making sure that each contains sufficient diversity of fault orientation to resolve the stress tensor. We refer to these as the northern, central, and southern zones (see Figure 1a). Synthetic tests show that each of the three stress domains contain sufficient diversity in the orientation of the observed slip vectors (see Figure S4 in Supporting Information S1) as they can all successfully recover a known stress tensor that is derived from seismicity (Hardebeck, 2020).

To invert the unit slip vectors for stress we use an iterative L_1 inversion because it is less sensitive to outliers than a standard L_2 least squares inversion (Aster et al., 2011). To minimize overfitting of the data and to constrain stress to be spatially smooth along the rupture we apply a damping constraint to the inversion that penalizes large changes of the stress orientation between neighboring zones (i.e., the gradients of the model vector between cells) (Hardebeck & Michael, 2006). The strength of the damping factor is estimated from the fall-off of the variance reduction curve because this approach is less ambiguous than a standard L-curve (Hreinsdóttir et al., 2006; Xu et al., 2016). The uncertainties of the stress model are then estimated from bootstrapping via random replacement of the original unit slip vectors.

2.3. Fault Friction and Absolute Stresses From Changes in Coseismic Slip

In our analysis we describe the relation between the fault instability (a term that characterizes how close a fault is to the failure envelope), stress drop and coseismic slip magnitude (see Figure 2 for illustration of variables used). This relation assumes a Mohr-Coulomb yielding criterion and constant stress drop within each of the three stress zones along the rupture ($\Delta\tau$) with no cohesion i.e., attributed to the pre-existing nature of the ruptured fault (Thompson Jobe et al., 2020). First, the stress drop is defined by the difference between the initial (τ_o, i.e., prior to the onset of seismic waves and the direct effect) and the dynamic shear stress (τ_d), which assumes the stress drop is uniform within each stress domain,

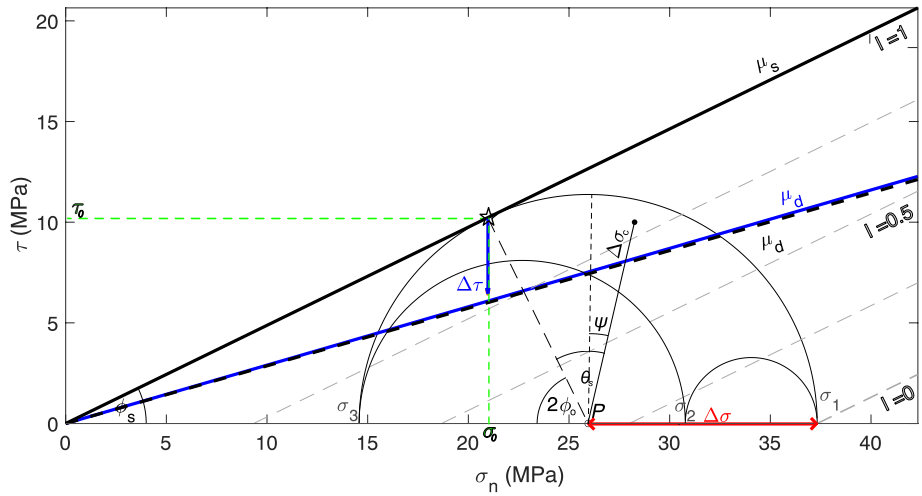

Figure 2. Mohr circle illustrating the variables used in Equations 1–18. Black filled circle shows the location in Mohr space of the state of stress on a plane with an arbitrary orientation. Effective normal stress is positive in compression (with values shown here only for illustrative purposes), and for illustration purposes positive shear stresses are parallel to dextral motion. Black solid line denotes the static friction (μ_s), black dashed and blue lines are dynamic friction (μ_d) estimated from the observed slip vector with lowest fault instability (I, gray lines) giving an upper bound to μ_d, and that inverted from our slip-fault instability model (red line in Figure 5d). Absolute stresses are estimated with knowledge of the maximum shear stress ($\Delta\sigma$) and mean horizontal stress (P). Internal angle of friction is ϕ_s, the angle between the failure plane and maximum principal stress (σ_1) is denoted by ϕ_o, the angle or deviation of an arbitrary failure plane (black dot) from the optimal angle with the failure envelope is shown by θ_s, with $\Delta\sigma_c$ denoting the stress differential from P that accounts for fault planes located away from the Mohr circle, the stress drop is shown by $\Delta\tau$, normal and shear stress on the critical failure plane is shown by σ_o and τ_o, respectively. The angle $\psi = \theta_s - \phi_s$.

$$\Delta\tau = \tau_0 - \tau_d$$

$$\Delta\tau = (\mu_s - \mu_d)\,\sigma_n', \tag{1}$$

where μ_s is the static friction, μ_d is the dynamic friction and σ_n' is the effective normal stress where the pore pressure is not specified. The effective normal stress for a fault of a given orientation can be expressed as (see Figure 2),

$$\sigma_n' = P + \Delta\sigma_c \cdot \sin(\theta_s - \phi_s)\,, \tag{2}$$

where ϕ_s is the angle of internal friction (i.e., $\arctan[\mu_s]$), and the angle θ_s is measured in degrees relative to the angle corresponding to the critical failure plane ϕ_s (where $\psi = \theta_s - \phi_s$ is represented in Figure 2). $\Delta\sigma_c$ is the distance in stress space, between the stress vector corresponding to the fault orientation and the center of the maximum Mohr circle. Because the intermediate principal stress is vertical, P is the mean horizontal stress. If the fault plane is vertical, the stress on that fault is located on the maximum Mohr circle and $\Delta\sigma_c$ is then equal to the maximum shear stress $\Delta\sigma$.

The shear stress along a given fault plane, τ can be expressed as

$$\tau = \Delta\sigma_c \cdot \cos(\theta_s - \phi_s)\,. \tag{3}$$

Equation 1 can then be re-written using Equations 2 and 3 as

$$\Delta\tau = \Delta\sigma_c \cdot \cos(\theta_s - \phi_s) - \mu_d\,(P + \Delta\sigma_c \cdot \sin[\theta_s - \phi_s])\,. \tag{4}$$

P can be expressed by the following and is represented geometrically in the lower left of Figure 2,

$$P = \frac{\Delta\sigma}{sin(\phi_s)}, \tag{5}$$

and from Equation 5 the stress drop can be re-written as,

$$\Delta\tau = \Delta\sigma_c \cdot \cos(\theta_s - \phi_s) - \mu_d \left[\frac{\Delta\sigma}{sin(\phi_s)} + \Delta\sigma_c \cdot \sin(\theta_s - \phi_s) \right]. \quad (6)$$

We can then re-write Equation 6 using the fault instability (I) (Vavryčuk et al., 2013), a term which quantifies how close to failure a fault is

$$I = \frac{\tau - \mu_s(\sigma_n' - 1)}{\mu_s + \sqrt{1 + \mu_s^2}}, \quad (7)$$

where the shear stress (τ) and effective normal stress (σ_n') are calculated from the normalized stress tensor and the fault orientation, and μ_s is an unknown quantity. This quantity characterizes the fault's proximity to failure based on its orientation, static friction, and the stress tensor. The value of I varies between 0 and 1, where higher values indicate faults that are more favorably oriented for failure. We re-write the fault instability as

$$I = \frac{\lambda\cos(\theta_s) + \sin(\phi_s)}{1 + \sin(\phi_s)}, \quad (8)$$

where $\lambda = \Delta\sigma_c/\Delta\sigma$ and solving for θ_s we find

$$\theta_s = \cos^{-1}\left(\frac{I + I \cdot sin[\phi_s] - sin[\phi_s]}{\lambda} \right). \quad (9)$$

We relate the average fault slip magnitude (D) to the stress drop as a function of the downdip rupture width (W), shear modulus (G) using,

$$D = \frac{W\Delta\tau}{CG}, \quad (10)$$

where C which is a geometrical term of 0.59 (estimated for a strike slip fault for the central zone with length (L) of 13 km measured from our deformation maps, Figure S1 in Supporting Information S1), with $(2/\pi)\sqrt{L/W}$ from Aki (1972). For the Ridgecrest rupture we assume a standard shear modulus $G = 30$ GPa that is consistent with the Southern California Earthquake Center community velocity model (Shaw et al., 2015; K. Wang et al., 2020) and a vertical rupture width $W = 15$ km, estimated from finite fault source models (Figure 1c) (K. Wang et al., 2020).

Using Equation 10 and Equation 6 we can now relate the coseismic slip magnitude to the orientation of each slip vector with respect to the stress field via

$$D = \frac{W}{CG} \cdot \left(\Delta\sigma_c \cdot \cos(\theta_s - \phi_s) - \mu_d \left[\frac{\Delta\sigma}{sin(\phi_s)} + \Delta\sigma_c \cdot \sin(\theta_s - \phi_s) \right] \right). \quad (11)$$

From Equation 8 the coseismic slip magnitude can then be related to the fault instability,

$$D = \frac{W}{CG} \cdot \left(\Delta\sigma_c \cdot \cos\left(\cos^{-1}\left(\frac{I + I \cdot sin[\phi_s] - sin[\phi_s]}{\lambda} \right) - \phi_s \right) - \mu_d \left[\frac{\Delta\sigma}{sin\phi_s} + \Delta\sigma_c \cdot \sin\left(\cos^{-1}\left(\frac{I + I \cdot sin[\phi_s] - sin[\phi_s]}{\lambda} \right) - \phi_s \right) \right] \right). \quad (12)$$

This quasi-static relation describes how the coseismic slip magnitude (D) varies depending on how optimally aligned a fault is relative to the stress field (I) and the amount of stress that is released due to the rupture. We can constrain most of the terms in Equation 12 to then estimate the frictional coefficients. As stated, W, C, and G are constrained quantities, while we determine $\Delta\sigma$ from measuring temporal stress rotations that occurred after the mainshock event. Specifically, $\Delta\sigma$ is estimated by comparing the orientation of the pre-mainshock stress state (determined from our slip vector inversion) with the post-mainshock stress orientation (derived from aftershocks) using the approach of Hardebeck and Hauksson (2001) (for details see Section 3.2 and Section S1 in Supporting Information S1). In addition, as we know the geometry of the faults and the normalized stress tensor from the slip vector inversion, we can estimate I by calculating the normalized shear and normalized effective normal stresses

from Equation 7. The slip magnitude, D, is measured along the rupture from our 3D surface deformation maps (see Figures 1a and 1b; Figures S1–S3 in Supporting Information S1). Therefore, as the only unknown quantities in Equation 12 are μ_d and μ_s (where the latter is related to I using Equation 7 and ϕ_s is the angle of internal friction), we can now use this relation to invert for the frictional coefficients.

To summarize, the relations described above assume that the magnitude of coseismic slip is determined by how much the shear stress drops from an initial value (τ_o) to a dynamic one (τ_d). This quasi-static approach assumes that the shear stress decreases to a constant dynamic value within each of the three stress zones (but can vary between them) as it is expected that sufficient sliding has occurred for the fault surface to be fully weakened and to have reached a steady-state dynamic friction as is observed in laboratory experiments carried out at seismic slip rates (Di Toro et al., 2011). Therefore, any variations of the slip magnitude within each of the zones along the rupture must then result from variations of the initial shear stress. We relate changes of the initial shear stress to changes of the fault orientation with respect to the ambient stress field. For example, faults that are well aligned to the stress field should have a higher initial shear stress, thereby giving a larger stress drop ($\tau_o - \tau_d$) and a larger slip magnitude compared to faults that are more orthogonal to σ_1, which would exhibit tractions with lower initial shear stress, a smaller shear stress change and therefore smaller slip amounts. Here we use the geometry of a restraining fault bend in this sense (see Figures 1a and 1b for location). This sensitivity of slip magnitude with the fault orientation (and thereby the initial stresses) is what we use to constrain the frictional properties of the ruptured faults. This sensitivity is introduced in our derivation above where we start from a simple quasi-static shear stress change (Equation 1) to a relation that includes the effect of a fault orientation that varies with the ambient stress field which acts to alter the traction on the fault surface (Equation 12). We apply this relation to the slip magnitude measured along the 19° restraining bend where quasi-static stress effects should be most significant.

From calculating μ_s using Equation 12, we can then calculate the angle of the fault (ϕ_o) at critical failure relative to the direction of the maximum compressive stress via the following

$$\phi_o = \frac{\pi}{4} - \frac{1}{2}\tan^{-1}(\mu_s)\,. \tag{13}$$

The initial shear stress at the point of failure (τ_0) can now be estimated by the following relation

$$\tau_0 = \Delta\sigma \cdot sin(2\phi_o)\,, \tag{14}$$

and is used to estimate the effective normal stress at the point of failure (σ_0'),

$$\sigma_0' = \frac{\tau_0}{\mu_s}. \tag{15}$$

The mean absolute horizontal stress (P) can now be estimated with Equation 5 or via the following,

$$P = \sigma_0' + \Delta\sigma \cdot \cos(2\phi_o)\,. \tag{16}$$

The absolute values of the principal stresses ($\sigma_i, i = 1, 2, 3$, where σ_1 is the maximum compressive stress) can then be calculated following,

$$\begin{aligned}\sigma_1 &= P + \Delta\sigma \\ \sigma_3 &= P - \Delta\sigma,\end{aligned} \tag{17}$$

and the intermediate compressive principal stress can be found using the shape ratio (R) derived from our slip vector inversion,

$$\sigma_2 = \sigma_1 - R\,(\sigma_1 - \sigma_3)\,. \tag{18}$$

3. Results

3.1. Deviatoric Stress Orientation

From inversion of the slip vector measurements across the three stress domains, we find the horizontal principal directions of the coseismic deviatoric stress tensor rotates ~12° eastward from south to north along the mainshock rupture

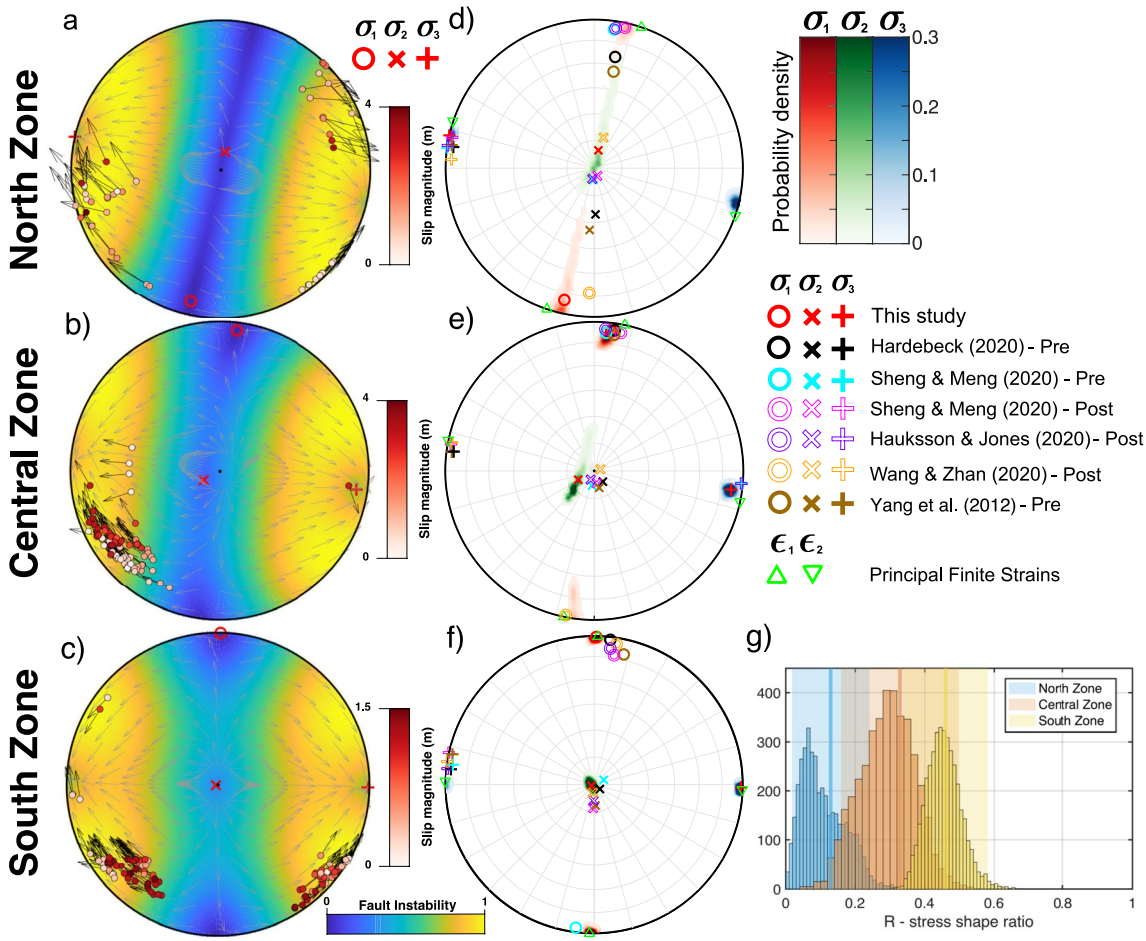

Figure 3. Stress state derived from inversion of coseismic slip vectors. Panels (a–c) show lower-hemisphere stress stereographs of the three stress zones, (a) is northern zone, (b) central zone, and (c) southern zone with the color background showing the fault instability (see Equations 7 and 8) and light gray vectors showing the predicted slip direction given by the stress model. Black vectors show the observed slip vectors where red-white colored dots denote the slip magnitude. Panels (d–f) show lower-hemisphere projection stereonets of the 3D stress tensor from our inversion (red symbols) with the uncertainties (colored regions) and other stress results from inverting background and postseismic seismicity (see key in top right). Finite principal strains (green triangles) are estimated from the optical displacement maps following approach of Milliner et al. (2021). (g) Distribution of R for the three zones, lower values indicate an increasingly transtensional stress regime. The vertical thick colored lines and transparent regions represent the mean R value and its 95% confidence interval for the background stress from Hardebeck (2020) for the three stress zones.

and becomes increasingly transtensional (see Figures 3d–3f). Here we find R decreases from 0.45 ± 0.05 in the south to 0.28 ± 0.08 in the central region and to 0.08 ± 0.06 in the north. Overall, the unit slip vectors predicted from the best-fitting stress model are very close to the observed coseismic unit slip vectors (illustrated by agreement of black and gray vectors in Figures 3a–3c) with a variance reduction of 96%, and a median angular misfit of 4°.

From measuring the relative orientation of coseismic Riedel and conjugate Riedel fractures that we identified from fault traces mapped at the surface by field surveys and high-resolution aerial imagery (Ponti et al., 2020; Rodriguez Padilla et al., 2022), we can estimate the horizontal direction of the maximum compressive stress (SH_{max}) that is independent of the SH_{max} expected by our stress model. Comparing the SH_{max} measured from the orientation of coseismic fractures with that predicted by our stress model shows a good agreement with a median angular misfit of $3.7 \pm 12.5°$ (see Figure 4; Section S2 in Supporting Information S1 for details). This is almost a factor of three improvement compared to a single-domain stress model where we would assume no spatial variability of the stress state along the rupture (see Figure S5 in Supporting Information S1). We also find that our stress results are robust given the number of zones chosen (for $n \leq 3$) for the inversion (Figures S5 and S6 in Supporting Information S1). In addition, our stress model shows a remarkable agreement with the pre-seismic stress tensor derived from previous studies using background seismicity (illustrated by symbols in Figures 3d–3f) (Hardebeck, 2020; Sheng & Meng, 2020; Yang et al., 2012).

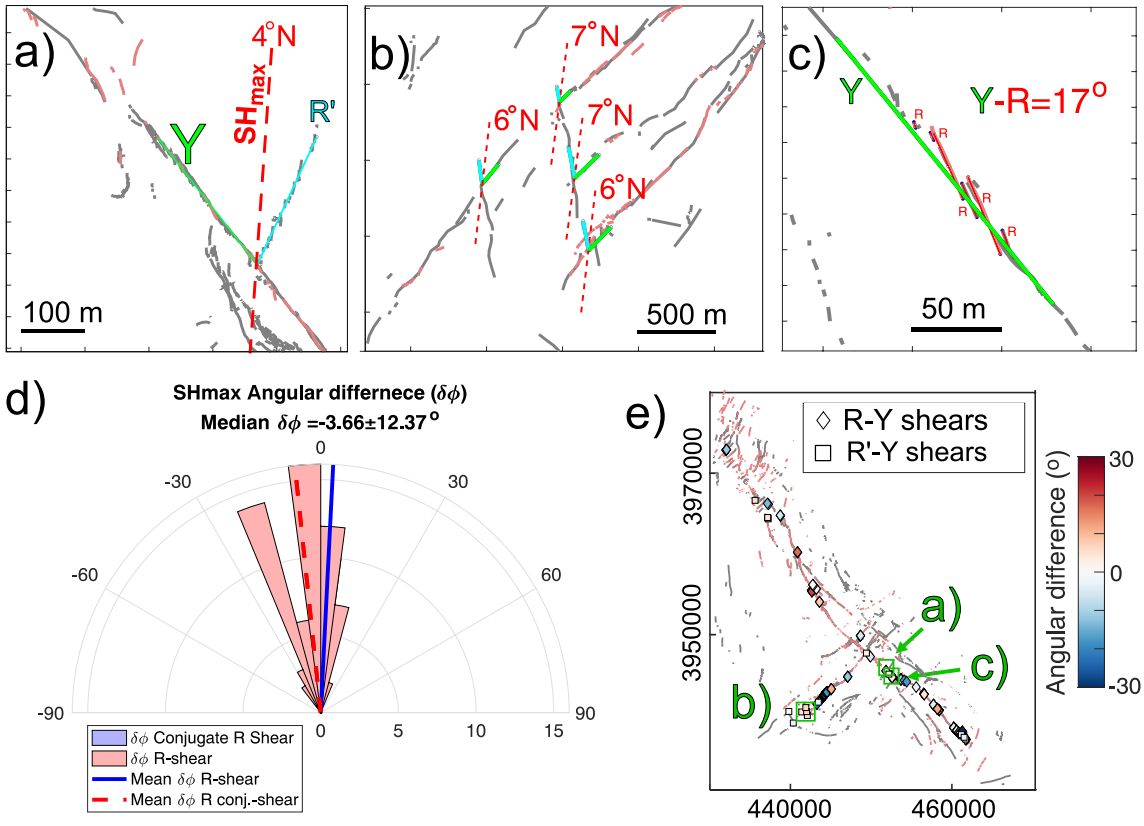

Figure 4. Validation of our stress model by comparison of SH_{max} measured from coseismic surface fractures. (a) Map view of an example of conjugate Riedel surface fractures (cyan lines) with through-going Y-shears (green) used to measure SH_{max} (dashed red line) along the southern portion of the mainshock rupture. Gray fault traces are from Ponti et al. (2020) and red from Rodriguez Padilla et al. (2022). (b) Map view of conjugate Riedel surface fractures (cyan lines) with through-going Y-shears (green) used to measure SH_{max} (dashed red line) along the southern portion of the foreshock rupture. (c) view of an example of Riedel surface fractures (red lines) with through-going Y-shears (green) used to measure SH_{max} along the southern portion of the mainshock rupture. Angle between Y-R shears shown in red. (d) Polar histogram of the overall angular difference between SH_{max} from our three-zone stress model with that measured from surface fractures (where R-Y fractures are shown in red and Y-R′ fractures shown in blue). (e) Map view shows location and magnitude of angular difference between SH_{max} from our three-zone stress model with that measured from surface fractures (where R-Y fractures are shown in diamonds and Y-R′ fractures plotted as squares).

3.2. Absolute Stress Magnitudes

We next calculate the magnitude of the deviatoric stress (characterized using the maximum shear stress $\Delta\sigma = [\sigma_1 - \sigma_3]/2$) within each zone from the rotation of the stress tensor before and after the Ridgecrest earthquakes following the approach of Hardebeck and Hauksson (2001). The stress rotation is estimated by comparing the stress tensor derived from our slip rake inversion, which we assume characterizes the initial pre-event stress state, with the stress orientation derived from aftershock focal mechanisms (Hauksson & Jones, 2020; Sheng & Meng, 2020; X. Wang & Zhan, 2020). This assumes that the stress orientation does not vary significantly as a function of depth. This assumption is supported by (a) a focal mechanism inversion analysis by Duan et al. (2022) that found no appreciable change in the orientation with depth and (b) the agreement of the pre-earthquake background stress state estimated from other studies using seismicity at depth with our own stress estimate (illustrated in Figures 3d–3f). Differences in the pre- and post-stress states show a temporal rotation of SH_{max} after the M_w 7.1 event, which we estimate as $-5.2 \pm 1.8°$, $1.3 \pm 1.2°$ and $7.0 \pm 1.2°$ (at the 1σ level, with clockwise as positive with respect to the primary ruptured faults) for the northern, central, and southern zones respectively (see Figure 5, Section S1 in Supporting Information S1 for details and Table 1). Using Equation S1 in Supporting Information S1 and the measured stress rotations gives $\Delta\sigma \approx 6.2$MPa for the northern zone, 9.0 MPa for the central zone (that includes the mainshock epicenter) and 2.0 MPa for the southern zone. To include the effects of the uncertainty of the stress tensor into the estimate of the frictional coefficients, we take the distribution of SH_{max}, that is derived from the stress tensor bootstrap sample (which has a 1σ variability of ~2°), and we propagate this uncer-

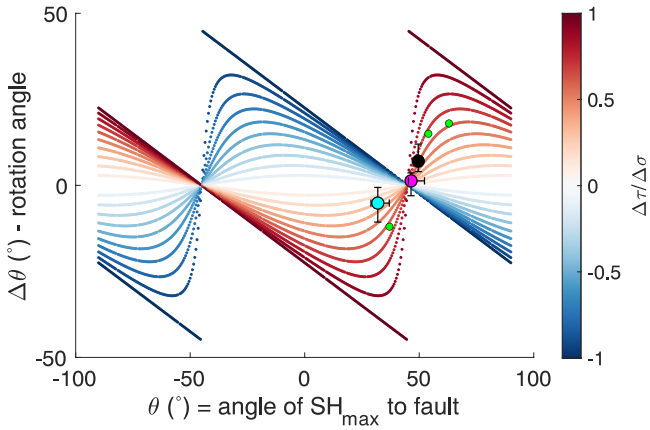

Figure 5. Estimate of absolute magnitude of maximum shear stresses. Cyan, magenta and black circles show the values for the north, central and southern stress zones, respectively, showing 95% confidence intervals. Small green circles show the values for the segments that ruptured during the 1992 M_w 7.3 Landers rupture from Hardebeck and Hauksson (2001). Ratio of the stress drop ($\Delta\tau$) to the maximum shear stress ($\Delta\sigma$) are plotted as smaller circles with red-blue color scale.

tainty through to get a distribution for the stress rotation, $\Delta\sigma$ and the static and dynamic frictional coefficients (see Figure S7 in Supporting Information S1 for the parameter distributions). We note the values of $\Delta\sigma$ are in the range of previous estimates following the 1992 M_w 7.3 Landers earthquake located further south in the Mojave Desert (shown by green dots in Figure 5) and agree with a deviatoric stress magnitude of 8 MPa estimated from stress rotations located near the epicenter of the M_w 7.1 Ridgecrest mainshock by Sheng and Meng (2020).

To estimate the absolute magnitude of the 3D principal stresses, the dynamic (μ_d) and static friction (μ_s) we assume a Mohr-Coulomb failure criterion and given that the faults ruptured in 2019 were pre-existing (Thompson Jobe et al., 2020) we assume that cohesion can be neglected. We apply the quasi-static analysis to the central zone, as it contains the transpressional fault-bend. From Equations 1–18 we find $\sigma_1 = 26.4$ MPa, $\sigma_2 = 21.2$ MPa, and $\sigma_3 = 8.3$ MPa (see Table 2 for stress tensor details). Given that σ_2 is vertical (Figures 3d–3f) and assuming an hydrostatic depth profile for the effective normal stress (with $\rho_c = 2,700\,\mathrm{kg/m^3}, \rho_w = 1,000\mathrm{kg/m^3}$), the stresses estimated here are representative of the top 1.3 km of the crust ($z = \sigma_2/[(\rho_c - \rho_w) * g]$). We note that in the occurrence of pressurized fluids in the crust, our hydrostatic assumption would mean the pore pressure stress profile and the representative depth (z) are underestimated. Therefore, the representative depth (z) should be considered as a lower bound estimate (i.e., the shallowest possible depth) in the occurrence of pressurized fluids in the crust.

3.3. Static and Dynamic Fault Friction

The slip tapering along the central bend of the main rupture occurs far from the southern end of the fault, where the rupture propagated for another 15 km along the southern segment beyond the bend. We therefore consider that the varying fault strike is the main cause of the tapering of slip along the transpressional bend. To test this hypothesis and understand its implications for fault friction we use the theoretical relation we derived between fault slip and fault instability (Equation 12) to solve for μ_s and μ_d. We determine the best-fitting values of $\mu_s = 0.61 \pm 0.14$ and μ_d to 0.29 ± 0.04 (black and blue line in Figure 6a, respectively) with the uncertainty estimated from a random replacement bootstrapping of the slip data. This variation of the slip magnitude as a function of the fault instability provides an excellent fit to the observations with a variance reduction of 98.14%, which captures the gradual decrease of slip magnitude with decreasing fault instability (red line in Figure 6d). Interestingly, the location of the fault at the epicenter in Mohr space (shown as the star in Figure 6a) is located very close to the failure envelope. This gives a stress drop at the failure point of $4.04 \pm A0.49$ MPa (shown by blue downward arrow in Figure 6a).

Given the stresses and friction now resolved along the rupture, we can compare how the coseismic slip magnitude varies as a function of the normalized normal and shear stress projected onto the fault. At each point along the rupture where we have an estimate of fault slip, we calculate the fault instability, I, as defined by Equations 7

Table 1
Parameters Used for Estimating Maximum Shear Stress ($\Delta\sigma$)

Stress zone	Pre SH_{max} orientation—this study (°)	Post SH_{max} (°)—Hauksson and Jones (2020)	Post SH_{max} (°)—Sheng and Meng (2020)	Post SH_{max} (°)—X. Wang and Zhan (2020)	Average Post SH_{max} (°)	Stress rotation (°)[a]	Average fault strike (°)	Average fault displacement (m)	$\Delta\sigma$ (MPa)
North	12.9 ± 1.8	8.72	12.3	2.23	7.75	−5.15	161	1.5	6.18
Central	7.56 ± 1.2	4.54	10.86	11.17	8.86	1.3	141.6	3.5	9.01
South	1.30 ± 1.2	6.89	8.9	9.23	8.34	7.04	131.73	1	2.01

[a]Positive values are clockwise rotations.

Table 2
Values Here Include the Stress Tensor Orientation in Polar Coordinates and Absolute Magnitudes, the Stress Shape Ratio (R), and the Static (μ_S) and Dynamic Friction (μ_d)

		σ_1		σ_2		σ_3				
Zone	N (stress/friction)	Tr/Pl (°)	MPa	Tr/Pl (°)	MPa	Tr/Pl (°)	MPa	R	μ_S	μ_d
North	46/–	192.8/10.0	22.0 ± 2.5	13.0/80.0	21.2 ± 2.5	282.8/0.1	9.7 ± 2.5	0.08 ± 0.06	–	–
Central	80/40	6.9/5.9	26.4 ± 2.5	241.1/80.0	21.2 ± 2.5	97.8/8.1	8.3 ± 2.5	0.28 ± 0.08	0.61 ± 0.14	0.29 ± 0.04
South	114/45	1.0/0.2	23.1 ± 2.5	259.2/88.9	21.2 ± 2.5	91.0/1.1	19.0 ± 2.5	0.45 ± 0.05	–	0.10 ± 0.04

Note. The first value of N denotes the number of slip vectors used in the inversion for stress (e.g., Figure 3), while the second denotes the number of slip vectors used in the inversion for friction (Equation 12, Figure 6). The latter are fewer because only slip along primary faults are used. Reported uncertainties are at the 1σ level.

and 8 (Vavryčuk, 2014; Vavryčuk et al., 2013). The fault instability and slip magnitude are both highest at the epicenter ($I > 0.9$ and slip = 4–5 m) and both decrease southwards along the 19° bend of the primary rupture (Figures 6b and 6c). Specifically, along the restraining bend the coseismic slip magnitude linearly decreases by as much as ∼2.5 m, from ∼3.8 m north of the bend to ∼1.2 m south of it (see Figure 1b). Similarly, we find the fault becomes more misorientated to the stress field from north-to-south along the bend (where SH_{max} is ∼N7°E), which is shown by a 27% decrease of the fault instability from ∼0.95 north of the bend to ∼0.68 south of it (see Figures 1b, 6b, 6c, and 7a).

The estimate of the dynamic friction ($\mu_d = 0.29 \pm 0.04$) agrees within the uncertainty but is slightly lower than an upper bound estimate of $\mu_d = 0.33$ derived from the state of stress on the fault segment with the lowest observed fault instability (black dashed line Figure 6a). Lastly, the static friction value that we invert for using the slip data ($\mu_s = 0.61 \pm 0.14$) is at the upper end of a prior estimate of $\mu_s = 0.4$–0.6 made by Fialko (2021) who used a different approach based on the dihedral angles of conjugate faults in the host rock surrounding the 2019 Ridgecrest rupture using seismicity lineations.

In Mohr stress space the relation of slip magnitude and fault instability is illustrated by larger slip values located closer to the failure envelope (where I is maximum at the failure envelope, Figure 6a). As a fault plane is located further away from the failure envelope and becomes increasingly mis-aligned to the stress field (i.e., I decreases), the slip magnitude measured within the central zone is found to gradually taper (red-white colored circles in Figure 6a), which is associated with a ∼10 MPa increase of the normal stresses and ∼1.5 MPa decrease of the shear stresses. Alternatively, this can be seen in the stereographs where higher slip is limited to the higher fault instability regions (Figures 3a–3c). We note that this comparison includes slip vectors only along the primary rupture strands and excludes points along shorter, parallel secondary faults, as the slip magnitude is expected to be limited by fault length. The northern zone is also consistent with this behavior of higher slip closer to the failure envelope and a decrease in magnitude away from it, but the northward tapering of slip could also be affected by the rupture termination (see Figure S8 in Supporting Information S1). Following our quasi-static assumption (Equation 12) we inverted the coseismic slip (D) for friction for both the central and southern zones (the northern zone lacks a sufficient range of slip magnitude to obtain robust values). Here we find appreciable differences in the frictional properties between the two stress zones (Figure 7a). To explain the observed slip magnitude in the southern zone and its variability given it occurred in a region of the crust with a lower maximum shear stress magnitude of $\Delta\sigma = 2.01$ MPa compared to the central zone ($\Delta\sigma = 9.01$ MPa, which are values determined from the stress rotations, see Table 1), the dynamic friction within the southern zone must have been significantly lower at $\mu_d = 0.10 \pm 0.04$ compared to the central zone ($\mu_d = 0.29 \pm 0.04$). However, we note that the variability in the slip magnitude within the southern zone could also be affected by dynamic stresses associated with the rupture termination that are not considered by our quasi-static assumption here. This is one reason why our analysis is focused on the central stress zone that is located away from the fault terminations and on the effect of a prominent 19° transpressional fault bend where the effect of quasi-static stresses are expected to be largest.

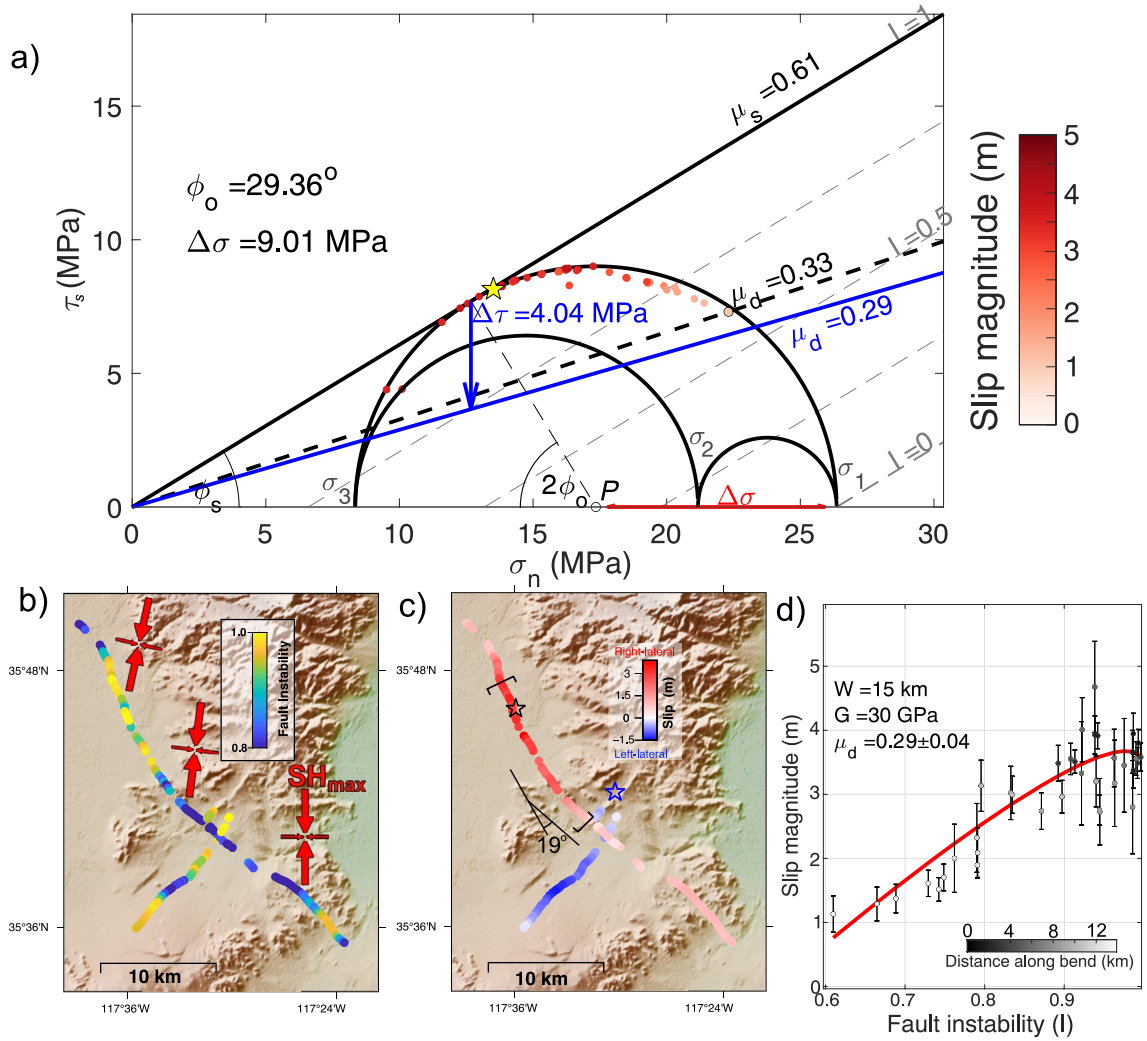

Figure 6. Relation between slip and fault instability. (a) Slip vectors in Mohr space of the central zone that contains the large-scale fault bend, with colors depicting the coseismic slip magnitude. Star shows the slip vector at the M_w 7.1 epicenter. Diagonal gray dashed lines show the fault instability (*I*), which decreases away from the failure envelope (Vavryčuk, 2014). Panel (b) illustrates variation of fault instability calculated from our best-fit 3D stress tensor (Figures 2d–2f) which shows a marked southwards decrease away from the M_w 7.1 mainshock epicenter, large red arrows denote SH_{max}. Panel (c) illustrates similar southward decrease of the observed coseismic slip magnitude (shown by red dots, note blue dots are also slip magnitude but with negative sign for left-lateral slip). Bend geometry of 19° is also illustrated and brackets along mainshock rupture show points used in friction inversion shown in (a) and (d). (d) Relation of *I* with observed slip magnitude along the central segments of the mainshock rupture with our best-fitting slip-fault instability model (red line, i.e., defined by Equation 12) giving a dynamic friction of 0.29 ± 0.04 (illustrated as blue line in a, with uncertainty determined from 4,000 bootstrap simulations of the data). Gray colorscale represents the distance of a point along the restraining bend, where 0 km denotes the most northwestern point along the mainshock rupture. This shows how both slip and *I* decrease from north-to-south along the fault bend.

4. Discussion

4.1. How Heterogenous Are Stresses in the Crust?

We conclude first that the assumption of a uniform stress field at the scale of the central zone (~13 km in length) can explain relatively well the tapering of slip (a decrease of ~2.5 m) along a 19° transpressional fault bend as it increases the effective normal stress and decreases the shear stress. This interpretation is in contrast with the suggestion that the slip tapering could have resulted from heterogeneities of static stress changes induced by the foreshock rupture (Chen et al., 2020; Cortez et al., 2021; Lozos & Harris, 2020; Zhang et al., 2020). The data show however some scatter around the model prediction which can reflect such heterogeneities of the initial stress. The scatter must also reflect the uncertainties on the measurements of the fault orientation and slip and heterogeneities of dynamic friction. Inertial effects during the rupture would also result in departure from the

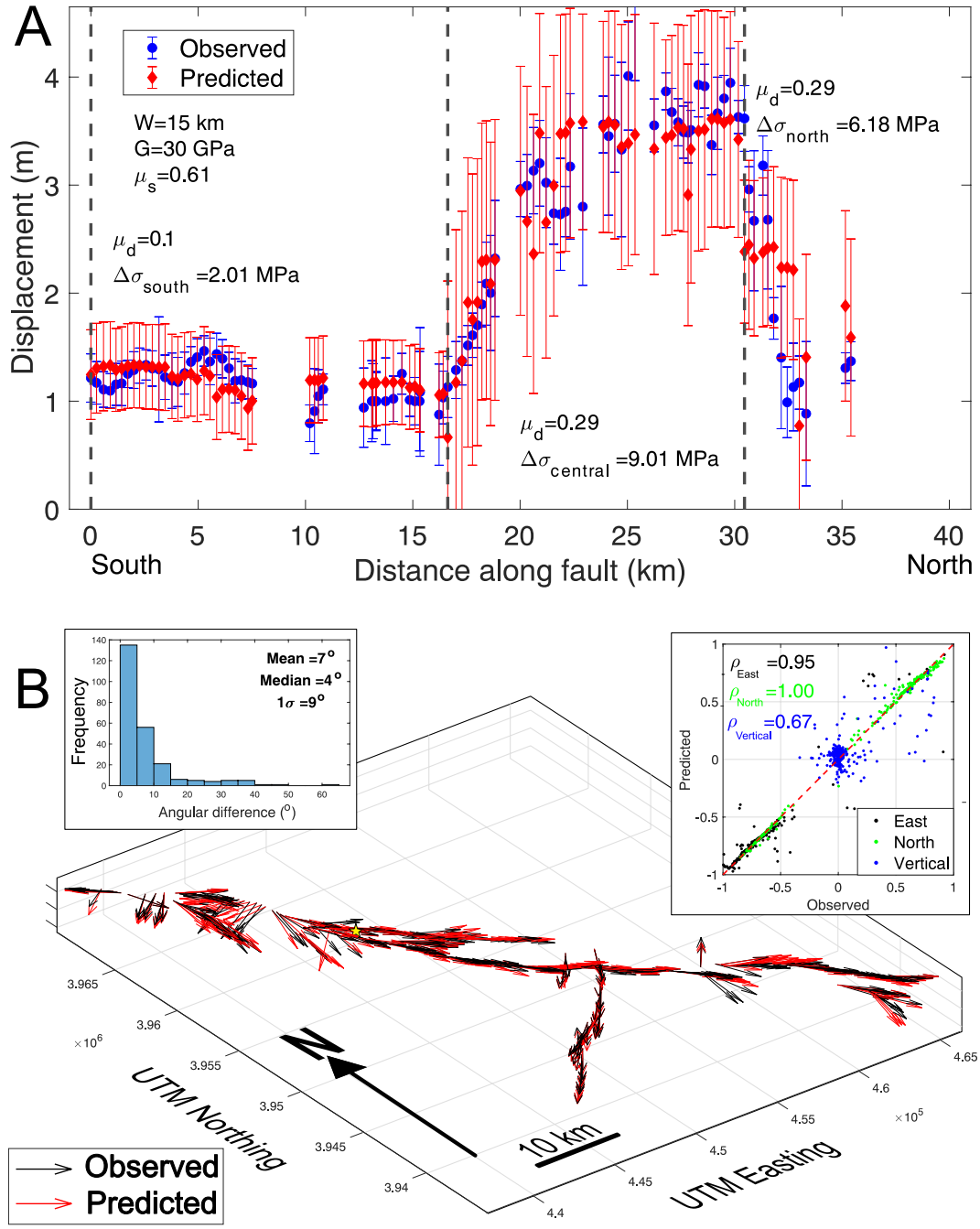

Figure 7. Comparison of the coseismic slip magnitude observed from image correlation with the predicted amount from our stress model (top) and the unit slip vector orientations (bottom). Panel (a) Coseismic slip profile along the mainshock rupture, viewing west, which compares geodetically observed coseismic slip magnitude (blue) with our quasi-static stress model prediction (red). Extent of the southern, central and northern stress zones are denoted by the black vertical dashed lines (see also Figure 1a for map view). Parameters for all three zones are shown in top left (where W, seismogenic width; G, shear modulus; μ_s, static friction), while the dynamic friction (μ_d) and the maximum shear stress ($\Delta\sigma$) are inverted separately for each stress domain (except the northern zone due to lack of data). (b) Upper left inset shows histogram of the angular difference in the slip rake between the observed and predicted slip vector for the best fitting three-zone stress model. Upper right inset is a correlation plot between the east-west (black dots), north-south (green dots) and vertical (blue dots) components of the unit slip vectors used in the stress inversion, labeled with the Pearson correlation coefficient (ρ) of each slip component. Bottom shows oblique map view comparing the observed 3D unit surface slip vectors (black) measured from the 3D image correlation result with those predicted (red vectors) from our best fitting stress model (also illustrated by stereographs in Figures 2a–2c), epicenter location is shown by yellow pentagram.

model prediction since Equation 12 assumes a quasistatic rupture process. Disentangling the various sources of misfits is therefore not straightforward. Heterogeneities of the stress field are however at least required when we compare the stress tensors derived for the three zones considered in our stress inversion. So, while stress heterogeneities must exist, they seem to play a subsidiary role in explaining the 2.5 m decrease in slip magnitude observed along the prominent rupture bend.

The stress orientation and its spatial variability is a key initial condition for physics-based numerical models to accurately simulate dynamic ruptures and the resulting strong ground motion (Graves et al., 2011; Olsen et al., 2009). Our inversion for the coseismic stress shows two features that change from south to north along the mainshock rupture. First, a 12° rotation of SH_{max} and the second, a ~50% decrease of the stress ratio indicating an increasingly transtensional stress regime in the direction toward the Basin and Range province. Both of these features are in strong agreement with the background pre-stress determined from pre-Ridgecrest focal mechanism seismicity (Hardebeck, 2020; Hauksson et al., 2020; Sheng & Meng, 2020; X. Wang & Zhan, 2020). Additional evidence to support the notion of a spatial variability in the stress field is that from south to north along the mainshock rupture the fault strike rotates eastward and becomes increasingly northward orientated which mimics the along-strike rotation of $SH_{max.}$ This change of the general fault strike may be a result of it adjusting over geologic timescales to become more optimally aligned to the change in SH_{max} direction.

Here we conclude that the background stresses inferred from seismicity provide a reasonable estimate of the initial stresses and that they can explain the first-order observed variability of coseismic slip along the rupture length (Figure 7). A forward calculation of the pre-mainshock stress state given by focal mechanism inversion of seismicity over the period before the 2019 Ridgecrest sequence (Hardebeck, 2020), shows it can explain a significant amount of the observed variability of the coseismic slip orientation along both the foreshock and mainshock ruptures (with a 92% variance reduction and a median angular difference of 6.77 ± 7.3, see Figure S9 in Supporting Information S1, which is similar to our best fitting stress model with a variance reduction of 95%, see Figure 7b). A close correspondence of the shear traction direction derived from the background stress with the coseismic slip rake was also found at seismogenic depths from estimates provided by a kinematic slip inversion of geodetic and seismologic data for the 2016 M_w 7.1 Kumamoto earthquake in Japan (Matsumoto et al., 2018). These results support the notion that a priori knowledge of the background stress and fault geometry can provide a reasonable constraint of the expected variation in the direction of coseismic slip (i.e., the rake) along a given fault system at the first-order, 5–10 km scale (while assuming no stress perturbations from other processes) (Figure 7b).

4.2. Fault Friction of Developing Faults Systems

The frictional resistance of faults is an important mechanical property that determines the level of shear stress faults can sustain. As faults are thought to structural evolve over time through strain localization and smoothing of the fault surface as they accumulate slip, the friction is thought to weaken (i.e., the level of shear stress that can be sustained is reduced) as different weakening mechanisms may start to take effect (Collettini et al., 2019; Noda et al., 2009; Renard et al., 2012; Rice, 2006; Sagy et al., 2007). The frictional strength of the faults that ruptured during the 2019 Ridgecrest earthquake sequence exhibit a strong Byerlee-type static strength ($\mu_s = 0.61 \pm 0.14$). Such a strong friction might not be surprising for an intra-crustal and immature fault system. An intermediate-strong frictional strength ($\mu_s = 0.4$–0.6) was however found by Fialko (2021) for smaller faults in the region surrounding the 2019 Ridgecrest earthquake sequence. A mechanism that was proposed to explain the lower frictional values is that long-term crustal tectonic rotation has progressively misaligned these relatively young faults to the ambient stress field, which in turn has weakened them and would indicate a frictional regime that is undergoing transition from an initially strong (e.g., $\mu_s = 0.60$) to a weak shear strength (Fialko, 2021; Fialko & Jin, 2021). The static friction we estimate here supports the notion of a classical static strength for an intra-crustal fault that is early in its structural and frictional development.

However, unlike immature faults, there is still debate regarding the frictional strength of mature plate-boundary fault systems. Specifically, whether mature faults are weak and sliding occurs at shear stresses well below the failure envelope predicted by Byerlee's law. The lack of a heat flow anomaly across the San Andreas fault and its possible mis-orientation to the background stress field have been proposed as evidence for mature faults having low frictional strength (Brune et al., 1969; Hardebeck & Michael, 2004; Lachenbruch & Sass, 1980; Rice, 1992; Scholz, 2000; Zoback et al., 1987). Although future work could address this still debated question by applying the

stress and friction analysis outlined here to forthcoming ruptures along mature fault systems, we envision it will be challenging to do so. The primary issue is that most mature fault systems have far simpler fault geometries closer to planar than immature faults. This would make it difficult to detect strong quasi-static stress effects induced by large geometrical changes such as fault bends, as these are needed to alter the normal and shear stresses and cause the required variation of slip (D) as a function of I to invert for the frictional parameters (Equation 12).

Lastly, we note that the stress change effects from the foreshock on the mainshock rupture segments are estimated to be small in the area of the fault bend that we are analyzing in this study and are unlikely to explain the decrease in coseismic slip along the fault bend (Lozos & Harris, 2020). The displacement points that we used in our frictional analysis are located away from the foreshock-mainshock junction, where stress changes are largest. The normal and shear stress effects in the near-surface are estimated to be <0.5 MPa along the bend that we analysis (Lozos & Harris, 2020). If we were to account for the small difference in these stress changes induced by the foreshock, this would have the effect of translating points in the Mohr space by a small amount (i.e., that in Figure 6a) and therefore would have a small effect on the frictional coefficient estimate.

4.3. Effect of Initial Stresses on Rupture Propagation

The unusually slow rupture of the mainshock was a notable feature of the M_w 7.1 mainshock event. Various mechanisms have been proposed to explain the ∼2 km/s rupture velocity including, a geometrically complex fault system (Goldberg et al., 2020) or stress unloading due to the M_w 6.4 foreshock (Chen et al., 2020). Dynamic rupture simulations have shown that fault bends can also affect the rupture velocity as the change in fault geometry alters the static initial stresses applied to the fault surface. It has been found for example, that restraining bends larger than 10° can decelerate the rupture substantially due to the locally larger initial normal stress (Kase & Day, 2006). More specific to the M_w 7.1 Ridgecrest earthquake, results from dynamic rupture modeling of Zhang et al. (2020) confirms a "stress barrier" effect due to high initial normal and low shear static stresses along the same fault bend that we study. Here our results are consistent with a change of the stresses projected onto the fault due to the variation of the fault's geometry along-strike. Our best fitting stress tensor shows that the 19° change in the fault orientation brought this rupture segment further away from an optimal alignment and closer to a perpendicular one with respect to the σ_1 direction (∼N7E°). This had the effect of decreasing the degree of optimal fault alignment by ∼27% (Figures 6b and 6d) and as we argue from our quasi-static analysis resulted in a ∼2.5 m decrease of coseismic slip (Figures 6c and 7a). Thus, our results support the occurrence of a significant increase in the initial normal stresses along the fault bend, which as expected from theoretical simulations, could have contributed to the unusually slow rupture propagation southwards and away from the mainshock epicenter.

Our analysis shows (a) that the initial shear stress along the fault bend seems primarily affected by the local fault strike (rather than spatial heterogeneities of the ambient stress field in the surrounding crust along the rupture at length scales <10 km), (b) that the slip rake is dictated by the pre-seismic shear stress direction, and (c) that the slip amplitude is dictated by the drop of initial shear stress to a uniform dynamic friction. We estimate $\mu_d = 0.29 \pm 0.04$ a value which is within the 0.05–0.4 range of steady-state dynamic friction measured in laboratory experiments at seismic slip rates on dry rocks (∼1 m/s) (Di Toro et al., 2011). The value of the fault instability for which the predicted slip is null according to our model provides an estimate of the maximum possible mis-orientation that would allow rupture propagation under quasi-static conditions. For $\mu_d = 0.29$ it means the orientation of reactivated faults must have an azimuth in the range between ∼8° and 66° from σ_1 (i.e., the range of ϕ limited by μ_d in Figure 6a) and that the magnitude of slip quickly diminishes as the fault orientation diverges from ∼30° as shown in Figures 6a and 6d and according to Equation 12. Fault misorientation was however not a key factor in arresting the rupture during the Ridgecrest mainshock. There are however examples of seismic ruptures that terminated where the fault becomes highly mis-oriented to the surrounding stress field. This includes the southern termination of the 1999 M_w 7.1 Hector Mine rupture (Hauksson et al., 2002) and the northern end of the 1992 M_w 7.3 Landers earthquake (Wollherr et al., 2019). In the case of the Landers earthquake, the rupture seems to have jumped from faults that became gradually misoriented to more optimally oriented faults leading to a highly segmented rupture (Bouchon, 1997).

The close correlation of coseismic slip magnitude with fault instability (Figure 6d) that is explained by our quasi-static model, shows that the slip magnitude and rake orientation could be estimated a priori by assuming a standard value of the static and dynamic friction, as well as the background stress orientation, deviatoric stress magnitude (or maximum shear stress) and the fault geometry (e.g., Figure 7). However, along-fault slip variability

has also been seen from other events and geomorphic analysis to correlate with the lateral fault segmentation, with local slip tapering on segments and slip troughs in inter-segment areas (Elliott et al., 2009; Klinger, 2010; Klinger et al., 2006; Manighetti et al., 2005; Milliner et al., 2016; Rockwell & Klinger, 2013). Such observations suggest that changes in fault orientation and stress that we show here are not the only mechanism to explain slip tapering along fault segments, which could also include variations in material properties, stress perturbations from prior ruptures, fault structural maturity and dynamic stresses amongst other effects (Bürgmann et al., 1994; Dieterich & Smith, 2010; Dunham et al., 2011; Perrin et al., 2016). Dynamic rupture simulations of the seismic cycle are however still needed to fully assess the effect of fault segmentation and fault termination.

5. Conclusions

Using a new 3D optical image correlation technique we have been able to capture the variations of the coseismic slip orientation and magnitude along a surface rupture at the hundreds of meters scale. These coseismic slip measurements can be explained by spatial variations of the stress field at the ten's of kilometer scale along the mainshock rupture, that is consistent with the known background stress state. From our analysis we show that for most of the rupture, co-seismic fault slip, is determined by the magnitude of the maximum shear stress in the surrounding crust ($\Delta\sigma$), the angle of the fault relative to the direction of the driving stress (characterized by the fault instability, I) and how much the frictional resistance of the fault surface decreases during sliding (i.e., the difference between μ_s and μ_d). By deriving a relation between these quantities and measuring them, where D is estimated from the surface deformation maps, $\Delta\sigma$ is measured from temporal stress rotations, and I is calculated from the known fault geometry and the normalized stress tensor (where the latter is itself determined from inverting the coseismic slip vectors), we are then able to invert for the static and dynamic frictional strength of the ruptured faults. We find the faults that ruptured are statically strong ($\mu_s = 0.61 \pm 0.14$) but dynamically weaken ($\mu_d = 0.29 \pm 0.04$). We note that this relationship holds only along fault segments where quasi-static stresses are larger than the dynamic stresses generated at the rupture tip, which is expected along large geometrical fault changes such as bends. We find this effect of the varying fault orientation with respect to the applied stress regime on the coseismic slip magnitude is consistent with theoretical predictions (Aochi et al., 2002; Kase & Day, 2006). The frictional analysis outlined here, opens up the possibility to constrain the absolute stress magnitudes and understand the degree of frictional strength and weakening that can occur during surface rupturing events along other fault systems with curved geometries exceeding tens of degrees.

Conflict of Interest

The authors declare no conflicts of interest relevant to this study.

Data Availability Statement

Optical Images were made available through NASA NGA commercial archive data service (https://cad4nasa.gsfc.nasa.gov/index.php), which is provided under the NextView license agreement. Maps were made using Generic Mapping Tools (https://www.generic-mapping-tools.org/). The COSI-Corr image correlation software can be accessed from (http://www.tectonics.caltech.edu/slip_history/spot_coseis/download_software.html). The measurements of the coseismic fault slip vectors, the 3D displacement maps and the MATLAB scripts to invert the coseismic slip vectors for the deviatoric stress tensor can be found from the Zenodo open repository https://doi.org/10.5281/zenodo.7162335.

Acknowledgments
We thank Jeanne Hardebeck, Xin Wang, Egill Hauksson and Shuzhong Sheng for making their stress results available. We thank Kim Olson, the editor Isabelle Manighetti, the associate editor and two anonymous reviewers for their comments and suggestions which helped strengthen the manuscript. We thank the NASA NGA commercial archive data service for access to the WorldView imagery (https://cad4nasa.gsfc.nasa.gov/index.php) which is provided under the NextView license agreement. This research was supported by the NASA Earth Surface and Interior focus area and performed at the Jet Propulsion Laboratory, California Institute of Technology (80NM0018D0004). Satellite imagery for this project were also purchased under SCEC Grant 19222.

References

Aati, S., Milliner, C., & Avouac, J.-P. (2022). A new approach for 2-D and 3-D precise measurements of ground deformation from optimized registration and correlation of optical images and ICA-based filtering of image geometry artifacts. *Remote Sensing of Environment*, *277*, 113038. https://doi.org/10.1016/j.rse.2022.113038

Aki, K. (1972). Earthquake mechanism. *Tectonophysics*, *13*(1–4), 423–446. https://doi.org/10.1016/0040-1951(72)90032-7

Andrew, J. E., & Walker, J. D. (2020). Total slip estimates of the M7.1 (July 2019) seismogenic Airport Lake fault system, Ridgecrest, California. In *2020 GSA Annual Meeting*.

Antoine, S. L., Klinger, Y., Delorme, A., Wang, K., Burgmann, R., & Gold, R. D. (2021). Diffuse deformation and surface faulting distribution from submetric image correlation along the 2019 Ridgecrest, California, ruptures. *Bulletin of the Seismological Society of America*, *111*(5), 2275–2302. https://doi.org/10.1785/0120210036

Aochi, H., Madariaga, R., & Fukuyama, E. (2002). Effect of normal stress during rupture propagation along nonplanar faults. *Journal of Geophysical Research*, *107*(B2), ESE 5-1–ESE 5-10. https://doi.org/10.1029/2001JB000500

Aster, R. C., Borchers, B., & Thurber, C. H. (2011). *Parameter estimation and inverse problems*. Academic Press.

Avouac, J. P., & Leprince, S. (2015). Geodetic imaging using optical systems. *Geodesy*, 387–424. https://doi.org/10.1016/B978-0-444-53802-4.00067-1

Barnhart, W. D., Hayes, G. P., & Gold, R. D. (2019). The July 2019 Ridgecrest, California, earthquake sequence: Kinematics of slip and stressing in cross-fault ruptures. *Geophysical Research Letters*, *46*(21), 11859–11867. https://doi.org/10.1029/2019GL084741

Bennett, R. A., Wernicke, B. P., Niemi, N. A., Friedrich, A. M., & Davis, J. L. (2003). Contemporary strain rates in the northern Basin and Range province from GPS data. *Tectonics*, *22*(2). https://doi.org/10.1029/2001TC001355

Besl, P. J., & McKay, N. D. (1992). A method for registration of 3-D shapes. *IEEE Transactions on Pattern Analysis and Machine Intelligence*, *14*(2), 239–256. https://doi.org/10.1109/34.121791

Bouchon, M. (1997). The state of stress on some faults of the San Andreas System as inferred from near-field strong motion data. *Journal of Geophysical Research*, *102*(B6), 11731–11744. https://doi.org/10.1029/97JB00623

Brune, J. N., Henyey, T. L., & Roy, R. F. (1969). Heat flow, stress, and rate of slip along the San Andreas Fault, California. *Journal of Geophysical Research*, *74*(15), 3821–3827. https://doi.org/10.1029/JB074i015p03821

Bürgmann, R., Pollard, D. D., & Martel, S. J. (1994). Slip distributions on faults: Effects of stress gradients, inelastic deformation, heterogeneous host-rock stiffness, and fault interaction. *Journal of Structural Geology*, *16*(12), 1675–1690. https://doi.org/10.1016/0191-8141(94)90134-1

Byerlee, J. (1978). Friction of rocks. In J. D. Byerlee & M. Wyss (Eds.), *Rock friction and earthquake prediction*. *Contributions to Current Research in Geophysics (CCRG)* (pp. 615–626). Birkhäuser. https://doi.org/10.1007/978-3-0348-7182-2_4

Chen, K., Avouac, J. P., Aati, S., Milliner, C., Zheng, F., & Shi, C. (2020). Cascading and pulse-like ruptures during the 2019 Ridgecrest earthquakes in the Eastern California Shear Zone. *Nature Communications*, *11*(1), 22. https://doi.org/10.1038/s41467-019-13750-w

Collettini, C., Tesei, T., Scuderi, M., Carpenter, B., & Viti, C. (2019). Beyond Byerlee friction, weak faults and implications for slip behavior. *Earth and Planetary Science Letters*, *519*, 245–263. https://doi.org/10.1016/j.epsl.2019.05.011

Cortez, J. T., Oglesby, D. D., Kyriakopoulos, C., Wu, B., Chaudhuri, K., Ghosh, A., & Douilly, R. (2021). On the rupture propagation of the 2019 M6.4 Searles Valley, California, earthquake, and the lack of immediate triggering of the M7.1 Ridgecrest earthquake. *Geophysical Research Letters*, *48*(4), e2020GL090659. https://doi.org/10.1029/2020GL090659

Dieterich, J. H., & Smith, D. E. (2010). Nonplanar faults: Mechanics of slip and off-fault damage. In Y. Ben-Zion & C. Sammis (Eds.), *Mechanics, structure and evolution of fault zones*. *Pageoph Topical Volumes* (pp. 1799–1815). Birkhäuser. https://doi.org/10.1007/978-3-0346-0138-2_12

Di Toro, G., Han, R., Hirose, T., De Paola, N., Nielsen, S., Mizoguchi, K., et al. (2011). Fault lubrication during earthquakes. *Nature*, *471*(7339), 494–498. https://doi.org/10.1038/nature09838

Dixon, T. H., Miller, M., Farina, F., Wang, H., & Johnson, D. (2000). Present-day motion of the Sierra Nevada block and some tectonic implications for the Basin and Range province, North American Cordillera. *Tectonics*, *19*(1), 1–24. https://doi.org/10.1029/1998TC001088

Duan, H., Chu, Z., Zhang, S., Yang, C., Chen, J., & Lei, J. (2022). Analysis of coseismic slip distributions and stress variations of the 2019 Mw 6.4 and 7.1 earthquakes in Ridgecrest, California. *Tectonophysics*, *831*, 229343. https://doi.org/10.1016/j.tecto.2022.229343

Dunham, E. M., Belanger, D., Cong, L., & Kozdon, J. E. (2011). Earthquake ruptures with strongly rate-weakening friction and off-fault plasticity, Part 2: Nonplanar faults. *Bulletin of the Seismological Society of America*, *101*(5), 2308–2322. https://doi.org/10.1785/0120100076

DuRoss, C. B., Gold, R. D., Dawson, T. E., Scharer, K. M., Kendrick, K. J., Akciz, S. O., et al. (2020). Surface displacement distributions for the July 2019 Ridgecrest, California, earthquake ruptures. *Bulletin of the Seismological Society of America*, *110*(4), 1400–1418. https://doi.org/10.1785/0120200058

Elliott, A. J., Dolan, J. F., & Oglesby, D. D. (2009). Evidence from coseismic slip gradients for dynamic control on rupture propagation and arrest through stepovers. *Journal of Geophysical Research*, *114*(B2), B02313. https://doi.org/10.1029/2008JB005969

Faulds, J. E., Henry, C. D., & Hinz, N. H. (2005). Kinematics of the northern Walker Lane: An incipient transform fault along the Pacific–North American plate boundary. *Geology*, *33*(6), 505–508. https://doi.org/10.1130/G21274.1

Fialko, Y. (2021). Estimation of absolute stress in the hypocentral region of the 2019 Ridgecrest, California, earthquakes. *Journal of Geophysical Research: Solid Earth*, *126*(7), e2021JB022000. https://doi.org/10.1029/2021JB022000

Fialko, Y., & Jin, Z. (2021). Simple shear origin of the cross-faults ruptured in the 2019 Ridgecrest earthquake sequence. *Nature Geoscience*, *14*(7), 513–518. https://doi.org/10.1038/s41561-021-00758-5

Fletcher, J. M., Oskin, M. E., & Teran, O. J. (2016). The role of a keystone fault in triggering the complex El Mayor–Cucapah earthquake rupture. *Nature Geoscience*, *9*(4), 303–307. https://doi.org/10.1038/ngeo2660

Gold, R. D., DuRoss, C. B., & Barnhart, W. D. (2021). Coseismic surface displacement in the 2019 Ridgecrest earthquakes: Comparison of field measurements and optical image correlation results. *Geochemistry, Geophysics, Geosystems*, *22*(3), e2020GC009326. https://doi.org/10.1029/2020GC009326

Goldberg, D. E., Melgar, D., Sahakian, V. J., Thomas, A. M., Xu, X., Crowell, B. W., & Geng, J. (2020). Complex rupture of an immature fault zone: A simultaneous kinematic model of the 2019 Ridgecrest, CA earthquakes. *Geophysical Research Letters*, *47*(3), e2019GL086382. https://doi.org/10.1029/2019GL086382

Graves, R., Jordan, T. H., Callaghan, S., Deelman, E., Field, E., Juve, G., et al. (2011). CyberShake: A physics-based seismic hazard model for southern California. *Pure and Applied Geophysics*, *168*(3), 367–381. https://doi.org/10.1007/s00024-010-0161-6

Gualandi, A., Serpelloni, E., & Belardinelli, M. E. (2016). Blind source separation problem in GPS time series. *Journal of Geodesy*, *90*(4), 323–341. https://doi.org/10.1007/s00190-015-0875-4

Hammond, W. C., & Thatcher, W. (2004). Contemporary tectonic deformation of the Basin and range province, western United States: 10 years of observation with the global positioning system. *Journal of Geophysical Research*, *109*(B8). https://doi.org/10.1029/2003JB002746

Hardebeck, J. L. (2020). A stress-similarity triggering model for aftershocks of the Mw 6.4 and 7.1 Ridgecrest earthquakes. *Bulletin of the Seismological Society of America*, *110*(4), 1716–1727. https://doi.org/10.1785/0120200015

Hardebeck, J. L., & Hauksson, E. (2001). Crustal stress field in southern California and its implications for fault mechanics. *Journal of Geophysical Research*, *106*(B10), 21859–21882. https://doi.org/10.1029/2001JB000292

Hardebeck, J. L., & Michael, A. J. (2004). Stress orientations at intermediate angles to the San Andreas Fault, California. *Journal of Geophysical Research*, *109*(B11), B11303. https://doi.org/10.1029/2004JB003239

Hardebeck, J. L., & Michael, A. J. (2006). Damped regional-scale stress inversions: Methodology and examples for southern California and the Coalinga aftershock sequence. *Journal of Geophysical Research*, *111*(B11). https://doi.org/10.1029/2005JB004144

Hauksson, E., & Jones, L. M. (2020). Seismicity, stress state, and style of faulting of the Ridgecrest-Coso region from the 1930s to 2019: Seismotectonics of an evolving plate boundary segment. *Bulletin of the Seismological Society of America*, *110*(4), 1457–1473. https://doi.org/10.1785/0120200051

Hauksson, E., Jones, L. M., & Hutton, K. (2002). The 1999 M_w 7.1 Hector Mine, California, earthquake sequence: Complex conjugate strike-slip faulting. *Bulletin of the Seismological Society of America*, *92*(4), 1154–1170. https://doi.org/10.1785/0120000920

Hauksson, E., Yoon, C., Yu, E., Andrews, J. R., Alvarez, M., Bhadha, R., & Thomas, V. (2020). Caltech/USGS Southern California Seismic Network (SCSN) and Southern California Earthquake Data Center (SCEDC): Data availability for the 2019 Ridgecrest sequence. *Seismological Research Letters*, *91*(4), 1961–1970. https://doi.org/10.1785/0220190290

Hreinsdóttir, S., Freymueller, J. T., Burgmann, R., & Mitchell, J. (2006). Coseismic deformation of the 2002 Denali Fault earthquake: Insights from GPS measurements. *Journal of Geophysical Research*, *111*(B3), B03308. https://doi.org/10.1029/2005JB003676

Kase, Y., & Day, S. M. (2006). Spontaneous rupture processes on a bending fault. *Geophysical Research Letters*, *33*(10). https://doi.org/10.1029/2006GL025870

Klinger, Y. (2010). Relation between continental strike-slip earthquake segmentation and thickness of the crust. *Journal of Geophysical Research*, *115*(B7), B07306. https://doi.org/10.1029/2009JB006550

Klinger, Y., Michel, R., & King, G. C. P. (2006). Evidence for an earthquake barrier model from Mw ~ 7.8 Kokoxili (Tibet) earthquake slip-distribution. *Earth and Planetary Science Letters*, *242*(3), 354–364. https://doi.org/10.1016/j.epsl.2005.12.003

Lachenbruch, A. H., & Sass, J. H. (1980). Heat flow and energetics of the San Andreas fault zone. *Journal of Geophysical Research*, *85*(B11), 6185–6222. https://doi.org/10.1029/JB085iB11p06185

Leprince, S., Ayoub, F., Klinger, Y., & Avouac, J. P. (2007). Co-registration of optically sensed images and correlation (COSI-Corr): An operational methodology for ground deformation measurements. In *2007 IEEE International Geoscience and Remote Sensing Symposium* (pp. 1943–1946). https://doi.org/10.1109/IGARSS.2007.4423207

Lozos, J. C., & Harris, R. A. (2020). Dynamic rupture simulations of the M6.4 and M7.1 July 2019 Ridgecrest, California, earthquakes. *Geophysical Research Letters*, *47*(7), e2019GL086020. https://doi.org/10.1029/2019GL086020

Manighetti, I., Campillo, M., Sammis, C., Mai, P. M., & King, G. (2005). Evidence for self-similar, triangular slip distributions on earthquakes: Implications for earthquake and fault mechanics. *Journal of Geophysical Research*, *110*(B5), B05302. https://doi.org/10.1029/2004JB003174

Matsumoto, S., Yamashita, Y., Nakamoto, M., Miyazaki, M., Sakai, S., Iio, Y., et al. (2018). Prestate of stress and fault behavior during the 2016 Kumamoto earthquake (M7.3). *Geophysical Research Letters*, *45*(2), 637–645. https://doi.org/10.1002/2017GL075725

McClusky, S. C., Bjornstad, S. C., Hager, B. H., King, R. W., Meade, B. J., Miller, M. M., et al. (2001). Present day kinematics of the eastern California shear zone from a geodetically constrained block model. *Geophysical Research Letters*, *28*(17), 3369–3372. https://doi.org/10.1029/2001GL013091

Michael, A. J. (1984). Determination of stress from slip data: Faults and folds. *Journal of Geophysical Research*, *89*(B13), 11517–11526. https://doi.org/10.1029/JB089iB13p11517

Milliner, C., & Donnellan, A. (2020). Using Daily observations from Planet Labs satellite imagery to separate the surface deformation between the 4 July Mw 6.4 foreshock and 5 July Mw 7.1 mainshock during the 2019 Ridgecrest earthquake sequence. *Seismological Research Letters*, *91*(4), 1986–1997. https://doi.org/10.1785/0220190271

Milliner, C., Donnellan, A., Aati, S., Avouac, J., Zinke, R., Dolan, J. F., et al. (2021). Bookshelf kinematics and the effect of dilatation on fault zone inelastic deformation: Examples from optical image correlation measurements of the 2019 Ridgecrest earthquake sequence. *Journal of Geophysical Research: Solid Earth*, *126*(3), e2020JB020551. https://doi.org/10.1029/2020JB020551

Milliner, C. W. D., Sammis, C., Allam, A. A., Dolan, J. F., Hollingsworth, J., Leprince, S., & Ayoub, F. (2016). Resolving fine-scale heterogeneity of co-seismic slip and the relation to fault structure. *Scientific Reports*, *6*(1), 27201. https://doi.org/10.1038/srep27201

Morelan, A. E., & Hernandez, J. L. (2020). Increasing postearthquake field mapping efficiency with optical image correlation. *Bulletin of the Seismological Society of America*, *110*(4), 1419–1426. https://doi.org/10.1785/0120200034

Nissen, E., Krishnan, A. K., Arrowsmith, J. R., & Saripalli, S. (2012). Three-dimensional surface displacements and rotations from differencing pre- and post-earthquake LiDAR point clouds. *Geophysical Research Letters*, *39*(16). https://doi.org/10.1029/2012GL052460

Noda, H., Dunham, E. M., & Rice, J. R. (2009). Earthquake ruptures with thermal weakening and the operation of major faults at low overall stress levels. *Journal of Geophysical Research*, *114*(B7), B07302. https://doi.org/10.1029/2008JB006143

Olsen, K. B., Day, S. M., Dalguer, L. A., Mayhew, J., Cui, Y., Zhu, J., et al. (2009). ShakeOut-D: Ground motion estimates using an ensemble of large earthquakes on the southern San Andreas fault with spontaneous rupture propagation. *Geophysical Research Letters*, *36*(4), L04303. https://doi.org/10.1029/2008GL036832

Perrin, C., Manighetti, I., Ampuero, J. P., Cappa, F., & Gaudemer, Y. (2016). Location of largest earthquake slip and fast rupture controlled by along-strike change in fault structural maturity due to fault growth. *Journal of Geophysical Research: Solid Earth*, *121*(5), 3666–3685. https://doi.org/10.1002/2015JB012671

Ponti, D. J., Blair, J. L., Rosa, C. M., Thomas, K., Pickering, A. J., Morelan, A., & Dawson, T. (2020). Digital datasets documenting surface fault rupture and ground deformation features produced by the Ridgecrest M6.4 and M7.1 earthquake sequence of July 4 and 5, 2019. *U.S. Geological Survey Data Release*. https://doi.org/10.5066/P9BZ5IJ9

Renard, F., Mair, K., & Gundersen, O. (2012). Surface roughness evolution on experimentally simulated faults. *Journal of Structural Geology*, *45*, 101–112. https://doi.org/10.1016/j.jsg.2012.03.009

Rice, J. R. (1992). Chapter 20 fault stress states, pore pressure distributions, and the weakness of the san Andreas fault. In B. Evans & T. Wong (Eds.), *International Geophysics*. *Fault Mechanics and Transport Properties of Rocks* (pp. 475–503). Academic Press. https://doi.org/10.1016/S0074-6142(08)62835-1

Rice, J. R. (2006). Heating and weakening of faults during earthquake slip. *Journal of Geophysical Research*, *111*(B5). https://doi.org/10.1029/2005JB004006

Rockwell, T. K., & Klinger, Y. (2013). Surface rupture and slip distribution of the 1940 Imperial Valley earthquake, Imperial fault, southern California: Implications for rupture segmentation and dynamics. *Bulletin of the Seismological Society of America*, *103*(2A), 629–640. https://doi.org/10.1785/0120120192

Rockwell, T. K., Lindvall, S., Herzberg, M., Murbach, D., Dawson, T., & Berger, G. (2000). Paleoseismology of the Johnson Valley, Kickapoo, and Homestead Valley faults: Clustering of earthquakes in the eastern California shear zone. *Bulletin of the Seismological Society of America*, *90*(5), 1200–1236. https://doi.org/10.1785/0119990023

Rodriguez Padilla, A. M., Oskin, M. E., Milliner, C. W. D., & Plesch, A. (2022). Accrual of widespread rock damage from the 2019 Ridgecrest earthquakes. *Nature Geoscience*, *15*(3), 222–226. https://doi.org/10.1038/s41561-021-00888-w

Ross, Z. E., Idini, B., Jia, Z., Stephenson, O. L., Zhong, M., Wang, X., et al. (2019). Hierarchical interlocked orthogonal faulting in the 2019 Ridgecrest earthquake sequence. *Science*, *366*(6463), 346–351. https://doi.org/10.1126/science.aaz0109

Sagy, A., Brodsky, E. E., & Axen, G. J. (2007). Evolution of fault-surface roughness with slip. *Geology*, *35*(3), 283–286. https://doi.org/10.1130/G23235A.1

Scholz, C. H. (2000). Evidence for a strong San Andreas fault. *Geology*, *28*(2), 163–166. https://doi.org/10.1130/0091-7613(2000)28<163:efassa>2.0.co;2

Shaw, J. H., Plesch, A., Tape, C., Suess, M. P., Jordan, T. H., Ely, G., et al. (2015). Unified structural representation of the southern California crust and upper mantle. *Earth and Planetary Science Letters*, *415*, 1–15. https://doi.org/10.1016/j.epsl.2015.01.016

Sheng, S., & Meng, L. (2020). Stress field variation during the 2019 Ridgecrest earthquake sequence. *Geophysical Research Letters*, *47*(15), e2020GL087722. https://doi.org/10.1029/2020GL087722

Thompson Jobe, J. A., Philibosian, B., Chupik, C., Dawson, T., K. Bennett, S. E., Gold, R., et al. (2020). Evidence of previous faulting along the 2019 Ridgecrest, California, earthquake ruptures. *Bulletin of the Seismological Society of America*, *110*(4), 1427–1456. https://doi.org/10.1785/0120200041

Vavryčuk, V. (2014). Iterative joint inversion for stress and fault orientations from focal mechanisms. *Geophysical Journal International*, *199*(1), 69–77. https://doi.org/10.1093/gji/ggu224

Vavryčuk, V., Bouchaala, F., & Fischer, T. (2013). High-resolution fault image from accurate locations and focal mechanisms of the 2008 swarm earthquakes in West Bohemia, Czech Republic. *Tectonophysics*, *590*, 189–195. https://doi.org/10.1016/j.tecto.2013.01.025

Wang, K., Dreger, D. S., Tinti, E., Burgmann, R., & Taira, T. (2020). Rupture process of the 2019 Ridgecrest, California Mw 6.4 foreshock and Mw 7.1 earthquake constrained by seismic and geodetic data. *Bulletin of the Seismological Society of America*, *110*(4), 1603–1626. https://doi.org/10.1785/0120200108

Wang, X., & Zhan, Z. (2020). Seismotectonics and fault geometries of the 2019 Ridgecrest sequence: Insight from aftershock moment tensor catalog using 3-D green's functions. *Journal of Geophysical Research: Solid Earth*, *125*(5), e2020JB019577. https://doi.org/10.1029/2020JB019577

Wesnousky, S. G. (2005). The San Andreas and Walker Lane fault systems, western North America: Transpression, transtension, cumulative slip and the structural evolution of a major transform plate boundary. *Journal of Structural Geology*, *27*(8), 1505–1512. https://doi.org/10.1016/j.jsg.2005.01.015

Wollherr, S., Gabriel, A.-A., & Mai, P. M. (2019). Landers 1992 "reloaded": Integrative dynamic earthquake rupture modeling. *Journal of Geophysical Research: Solid Earth*, *124*(7), 6666–6702. https://doi.org/10.1029/2018JB016355

Xu, X., Tong, X., Sandwell, D. T., Milliner, C. W., Dolan, J. F., Hollingsworth, J., et al. (2016). Refining the shallow slip deficit. *Geophysical Journal International*, *204*(3), 1867–1886. https://doi.org/10.1093/gji/ggv563

Yang, W., Hauksson, E., & Shearer, P. M. (2012). Computing a large refined catalog of focal mechanisms for southern California (1981–2010): Temporal stability of the style of faulting. *Bulletin of the Seismological Society of America*, *102*(3), 1179–1194. https://doi.org/10.1785/0120110311

Zhang, Z., Zhang, W., Xin, D., Chen, K., & Chen, X. (2020). A dynamic-rupture model of the 2019 Mw 7.1 Ridgecrest earthquake being compatible with the observations. *Seismological Research Letters*, *92*(2A), 870–876. https://doi.org/10.1785/0220200258

Zoback, M. D., Zoback, M. L., Mount, V. S., Suppe, J., Eaton, J. P., Healy, J. H., et al. (1987). New evidence on the state of stress of the San Andreas fault system. *Science*, *238*(4830), 1105–1111. https://doi.org/10.1126/science.238.4830.1105